

1 **Assessing the simulated soil hydrothermal regime of active layer**  
2 **from Noah-MP LSM v1.1 in the permafrost regions of the**  
3 **Qinghai-Tibet Plateau**

4

5 Xiangfei Li<sup>1,2</sup>, Tonghua Wu<sup>1,\*</sup>, Xiaodong Wu<sup>1</sup>, Jie Chen<sup>1</sup>, Xiaofan Zhu<sup>1</sup>, Guojie Hu<sup>1</sup>,  
6 Ren Li<sup>1</sup>, Yongping Qiao<sup>1</sup>, Cheng Yang<sup>1,2</sup>, Junming Hao<sup>1,2</sup>, Jie Ni<sup>1,2</sup>, Wensi Ma<sup>1,2</sup>

7

8 <sup>1</sup> Cryosphere Research Station on the Qinghai-Tibet Plateau, State Key Laboratory of  
9 Cryospheric Science, Northwest Institute of Eco-Environment and Resources, Chinese  
10 Academy of Sciences, Lanzhou 730000, China

11 <sup>2</sup> University of Chinese Academy of Sciences, Beijing 100049, China

12

13 **Correspondence:** Tonghua Wu (thuawu@lzb.ac.cn)

14

15 **Abstract.** Extensive and rigorous model inter-comparison is of great importance before  
16 application due to the uncertainties in current land surface models (LSMs). Without  
17 considering the uncertainties of forcing data and model parameters, this study designed  
18 an ensemble of 55296 experiments to evaluate the Noah land surface model with multi-  
19 parameterization (Noah-MP) for snow cover events (SCEs), soil temperature (ST) and  
20 soil liquid water (SLW) simulation, and investigated the sensitivity of parameterization  
21 schemes at a typical permafrost site on the Qinghai-Tibet Plateau. The results showed  
22 that Noah-MP systematically overestimates snow cover, which could be greatly  
23 resolved when adopting the sublimation from wind and semi-implicit snow/soil  
24 temperature time scheme. As a result of the overestimated snow, Noah-MP generally  
25 underestimates ST and is mostly influenced by the snow process. Systematic cold bias  
26 and large uncertainties of soil temperature remains after eliminating the effects of snow,  
27 particularly at the deep layers and during the cold season. The combination of roughness  
28 length for heat and under-canopy aerodynamic resistance contributes to resolve the cold  
29 bias of soil temperature. In addition, Noah-MP generally underestimates top SLW. The  
30 RUN process dominates the SLW simulation in comparison of the very limited impacts  
31 of all other physical processes. The analysis of the model structural uncertainties and  
32 characteristics of each scheme would be constructive to a better understanding of the  
33 land surface processes in the permafrost regions of the QTP and further model  
34 improvements towards soil hydrothermal regime modeling using the LSMs.  
35

## 36 1 Introduction

37 The Qinghai-Tibet Plateau (QTP) is underlain by the world's largest high-altitude  
38 permafrost covering a contemporary area of  $1.06 \times 10^6$  km<sup>2</sup> (Zou et al., 2017). Under  
39 the background of climate warming and intensifying human activities, soil  
40 hydrothermal dynamics in the permafrost regions on the QTP has been widely suffering  
41 from soil warming (Wang et al., 2021), soil wetting (Zhao et al., 2019), and changes in  
42 soil freeze-thaw cycle (Luo et al., 2020). Such changes has not only induced the  
43 reduction of permafrost extent, disappearing of permafrost patches and thickening of  
44 active layer (Chen et al., 2020), but also resulted in alterations in hydrological cycles  
45 (Zhao et al., 2019; Woo, 2012), changes of ecosystem (Fountain et al., 2012; Yi et al.,  
46 2011) and damages to infrastructures (Hjort et al., 2018). Therefore, it is very important  
47 to monitor and simulate the soil hydrothermal regime to adapt to the changes taking  
48 place.

49 A number of monitoring sites have been established in the permafrost regions of  
50 the QTP (Cao et al., 2019). However, it is inadequate to construct the soil hydrothermal  
51 state by considering the spatial variability of the ground thermal regime and an uneven  
52 distribution of these observations. In contrast, numerical models are competent  
53 alternatives. In recent years, land surface models (LSMs), which describe the exchanges  
54 of heat, water, and momentum between the land and atmosphere (Maheu et al., 2018),  
55 have received significant improvements in the representation of permafrost and frozen  
56 ground processes (Koven et al., 2013; Nicolsky et al., 2007; Melton et al., 2019). LSMs  
57 are capable of simulating the transient change of subsurface hydrothermal processes  
58 (e.g. soil temperature and moisture) with soil heat conduction (-diffusion) and water  
59 movement equations (Daniel et al., 2008). Moreover, they could be integrated with the  
60 numerical weather prediction system like WRF (Weather Research and Forecasting),  
61 making them as effective tools for comprehensive interactions between climate and  
62 permafrost (Nicolsky et al., 2007).

63 Some LSMs have been evaluated and applied in the permafrost regions of the QTP.  
64 Guo and Wang (2013) investigated near-surface permafrost and seasonally frozen

65 ground states as well as their changes using the Community Land Model, version 4  
66 (CLM4). Hu et al. (2015) applied the coupled heat and mass transfer model to identify  
67 the hydrothermal characteristics of the permafrost active layer in the Qinghai-Tibet  
68 Plateau. Using an augmented Noah LSM, Wu et al. (2018) modeled the extent of  
69 permafrost, active layer thickness, mean annual ground temperature, depth of zero  
70 annual amplitude and ground ice content on the QTP in 2010s. Despite those  
71 achievements based on different models, LSMs are in many aspects insufficient in  
72 permafrost regions. For one thing, large uncertainties still exist in the state-of-the-art  
73 LSMs when simulating the soil hydrothermal regime on the QTP (Chen et al., 2019).  
74 For instance, 19 LSMs in CMIP5 overestimate snow depth over the QTP (Wei and Dong,  
75 2015), which could result in the variations of the soil hydrothermal regime in the aspects  
76 of magnitude and vector (cooling or warming) (Zhang, 2005). Moreover, most of the  
77 existing LSMs are not originally developed for permafrost regions. Many of their soil  
78 processes are designed for shallow soil layers (Westermann et al., 2016), but permafrost  
79 would occur in the deep soil. And the soil column is often considered homogeneous,  
80 which cannot represent the stratified soil common on the QTP (Yang et al., 2005). Given  
81 the numerous LSMs and possible deficiencies, it is necessary to assess the  
82 parameterization schemes for permafrost modeling on the QTP, which is helpful to  
83 identify the influential sub-processes, enhance our understanding of model behavior,  
84 and guide the improvement of model physics (Zhang et al., 2016).

85 Noah land surface model with multi-parameterization (Noah-MP) provides a  
86 unified framework in which a given physical process can be interpreted using multiple  
87 optional parameterization schemes (Niu et al., 2011). Due to the simplicity in selecting  
88 alternative schemes within one modeling framework, it has been attracting increasing  
89 attention in inter-comparison work among multiple parameterizations at point and  
90 watershed scales (Hong et al., 2014; Zheng et al., 2017; Gan et al., 2019; Zheng et al.,  
91 2019; Chang et al., 2020; You et al., 2020). For example, Gan et al. (2019) carried out  
92 an ensemble of 288 simulations from multi-parameterization schemes of six physical  
93 processes, assessed the uncertainties of parameterizations in Noah-MP, and further

94 revealed the best-performing schemes for latent heat, sensible heat and terrestrial water  
95 storage simulation over ten watersheds in China. You et al. (2020) assessed the  
96 performance of Noah-MP in simulating snow process at eight sites over distinct snow  
97 climates and identified the shared and specific sensitive parameterizations at all sites,  
98 finding that sensitive parameterizations contribute most of the uncertainties in the  
99 multi-parameterization ensemble simulations. Nevertheless, there is little research on  
100 the inter-comparison of soil hydrothermal processes in the permafrost regions. In this  
101 study, an ensemble experiment of totally 55296 scheme combinations was conducted  
102 at a typical permafrost monitoring site on the QTP. The simulated snow cover events  
103 (SCEs), soil temperature (ST) and soil liquid water (SLW) of Noah-MP model was  
104 assessed and the sensitivities of parameterization schemes at different depths were  
105 further investigated. This study could be expected to present a reference for soil  
106 hydrothermal simulation in the permafrost regions on the QTP.

107 This article is structured as follows: Section 2 introduces the study site,  
108 atmospheric forcing data, design of ensemble simulation experiments, and sensitivity  
109 analysis methods. Section 3 describes the ensemble simulation results of SCEs, ST and  
110 SLW, explores the sensitivity and interactions of parameterization schemes. Section 4  
111 discusses the schemes in each physical process. Section 5 concludes the main findings.

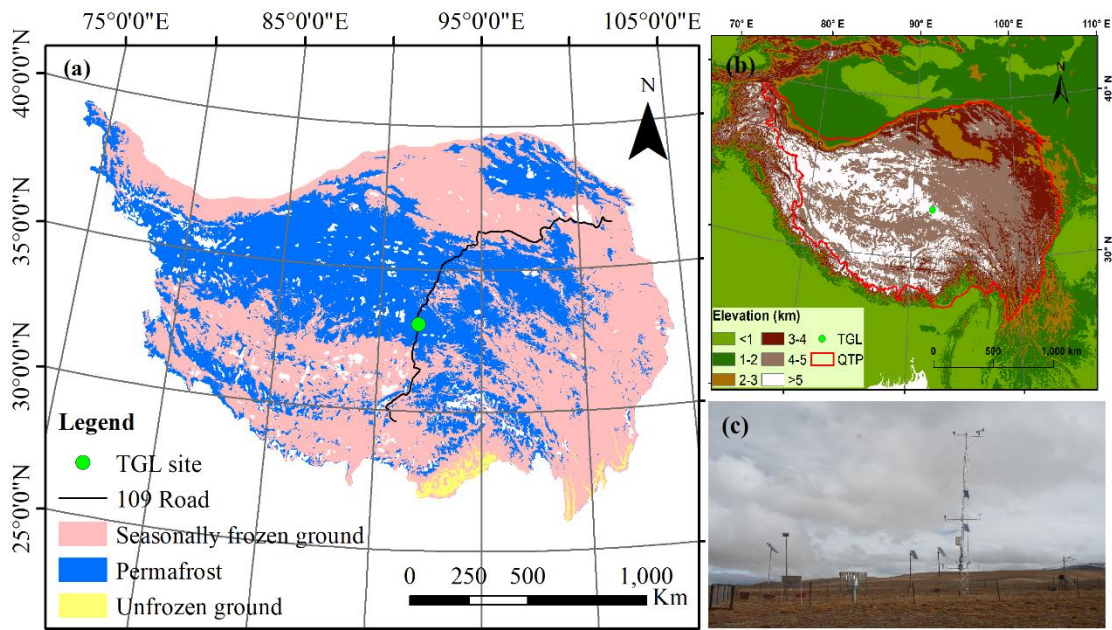
## 112 **2 Methods and materials**

### 113 **2.1 Site description and observation datasets**

114 Tanggula observation station (TGL) lies in the continuous permafrost regions of  
115 Tanggula Mountain, central QTP (33.07°N, 91.93°E, Alt.: 5,100 m a.s.l; Fig. 1). This  
116 site a typical permafrost site on the plateau with sub-frigid and semiarid climate (Li et  
117 al., 2019), filmy and discontinuous snow cover (Che et al., 2019), sparse grassland (Yao  
118 et al., 2011), coarse soil (Wu and Nan, 2016; He et al., 2019), and thick active layer  
119 (Luo et al., 2016), which are common features in the permafrost regions of the plateau.  
120 According to the observations from 2010–2011, the annual mean air temperature of

121 TGL site was  $-4.4\text{ }^{\circ}\text{C}$ . The annual precipitation was 375 mm, and of which 80% is  
 122 concentrated between May and September. Alpine steppe with low height is the main  
 123 land surface, whose coverage range is about 40% ~ 50% (Yao et al., 2011). The active  
 124 layer thickness is about 3.15 m (Hu et al., 2017).

125 The atmospheric forcing data, including wind speed/direction, air  
 126 temperature/relative humidity/pressure, downward shortwave/longwave radiation, and  
 127 precipitation, were used to drive the model. These variables above were measured at a  
 128 height of 2 m and covered the period from August 10, 2010 to August 10, 2012 (Beijing  
 129 time) with a temporal resolution of 1 hour. Daily soil temperature and liquid moisture  
 130 at depths of 5cm, 25cm, 70cm, 140cm, 220cm and 300cm from August 10, 2010 to  
 131 August 9, 2011 (Beijing time) were utilized to validate the simulation results.



132  
 133 **Figure 1.** Location and geographic features of study site. (a) Location of observation  
 134 site and permafrost distribution (Zou et al., 2017). (b) Topography of the Qinghai-Tibet  
 135 Plateau. (c) Photo of the Tanggula observation station.

## 136 2.2 Ensemble experiments of Noah-MP

137 The offline Noah-MP LSM v1.1 was assessed in this study. The default Noah-MP  
 138 consists of 12 physical processes that are interpreted by multiple optional

139 parameterization schemes. These sub-processes include vegetation model (VEG),  
140 canopy stomatal resistance (CRS), soil moisture factor for stomatal resistance (BTR),  
141 runoff and groundwater (RUN), surface layer drag coefficient (SFC), super-cooled  
142 liquid water (FRZ), frozen soil permeability (INF), canopy gap for radiation transfer  
143 (RAD), snow surface albedo (ALB), precipitation partition (SNF), lower boundary of  
144 soil temperature (TBOT) and snow/soil temperature time scheme (STC) (Table 1).  
145 Details about the processes and optional parameterizations can be found in Yang et al.  
146 (2011a).

147 VEG(1) is adopted in the VEG process, in which the vegetation fraction is  
148 prescribed according to the NESDIS/NOAA 0.144 degree monthly 5-year climatology  
149 green vegetation fraction (<https://www.emc.ncep.noaa.gov/mmb/gcip.html>), and the  
150 monthly leaf area index (LAI) was derived from the Advanced Very High-Resolution  
151 Radiometer (AVHRR) (<https://www.ncei.noaa.gov/data/>, Claverie et al., 2016).  
152 Previous studies has confirmed that Noah-MP seriously overestimate the snow events  
153 and underestimate soil temperature and moisture on the QTP (Jiang et al., 2020; Li et  
154 al., 2020; Wang et al., 2020), which can be greatly resolved by considering the  
155 sublimation from wind (Gordon scheme) and a combination of roughness length for  
156 heat and under-canopy aerodynamic resistance (Y08-UCT) (Zeng et al., 2005; Yang et  
157 al., 2008; Li et al., 2020). For a more comprehensive assessment, we added two physical  
158 processes based on the default Noah-MP model, i.e. the snow sublimation from wind  
159 (SUB) and the combination scheme process (CMB) (Table 1). In the two processes,  
160 users can choose to turn on the Gordon and Y08-UCT scheme (described in the study  
161 of Li et al., 2020) or not. As a result, in total 55296 combinations are possible for the  
162 13 processes and orthogonal experiments were carried out to evaluate their performance  
163 in soil hydrothermal dynamics and obtain the optimal combination.

164 The Noah-MP model was modified to consider the vertical heterogeneity in the  
165 soil profile by setting the corresponding soil parameters for each layer. The soil  
166 hydraulic parameters, including the porosity, saturated hydraulic conductivity,  
167 hydraulic potential, the Clapp-Hornberger parameter b, field capacity, wilt point, and

168 saturated soil water diffusivity, were determined using the pedotransfer functions  
 169 proposed by Hillel (1980), Cosby et al. (1984), and Wetzel and Chang (1987)  
 170 (Equations S1-S7), in which the sand and clay percentages were based on Hu et al.,  
 171 (2017) (Table S1). In addition, the simulation depth was extended to 8.0 m to cover the  
 172 active layer thickness of the QTP. The soil column was discretized into 20 layers, whose  
 173 depths follow the default scheme in CLM 5.0 (Table S1, Lawrence et al., 2018). Due to  
 174 the inexact match between observed and simulated depths, the simulations at 4cm,  
 175 26cm, 80cm, 136cm, 208cm and 299cm were compared with the observations at 5cm,  
 176 25cm, 70cm, 140cm, 220cm and 300cm, respectively. A 30-year spin-up was conducted  
 177 in every simulation to reach equilibrium soil states.

178 **Table 1.** The physical processes and options of Noah-MP.

| Physical processes                                 | Options   |
|--|---|
| Vegetation model (VEG)                             | (1) table LAI, prescribed vegetation fraction<br>(2) dynamic vegetation<br>(3) table LAI, calculated vegetation fraction<br>(4) table LAI, prescribed max vegetation fraction |
| Canopy stomatal resistance (CRS)                   | (1) Jarvis<br>(2) Ball-Berry  |
| Soil moisture factor for stomatal resistance (BTR) | (1) Noah<br>(2) CLM<br>(3) SSiB   |
| Runoff and groundwater (RUN)                       | (1) SIMGM with groundwater<br>(2) SIMTOP with equilibrium water table<br>(3) Noah (free drainage)<br>(4) BATS (free drainage)   |
| Surface layer drag coefficient (SFC)               | (1) Monin-Obukhov (M-O)<br>(2) Chen97   |
| Super-cooled liquid water (FRZ)                    | (1) generalized freezing-point depression<br>(2) Variant freezing-point depression  |
| Frozen soil permeability (INF)                     | (1) Defined by soil moisture, more permeable<br>(2) Defined by liquid water, less permeable   |
| Canopy gap for radiation transfer (RAD)            | (1) Gap=F(3D structure, solar zenith angle)<br>(2) Gap=zero<br>(3) Gap=1-vegetated fraction   |
| Snow surface albedo (ALB)                          | (1) BATS<br>(2) CLASS   |
| Precipitation partition (SNF)                      | (1) Jordan91<br>(2) BATS: $T_{sfc} < T_{frz} + 2.2K$<br>(3) $T_{sfc} < T_{frz}$   |



|   |  |
|---|--|
| Lower boundary of soil temperature (TBOT)   | (1) zero heat flux<br>(2) soil temperature at 8m depth |
| Snow/soil temperature time scheme (STC)     | (1) semi-implicit<br>(2) full implicit                 |
| Snow sublimation from wind (SUB)            | (1) No (2) Yes   |
| Combination scheme by Li et al.(2020) (CMB) | (1) No (2) Yes   |

---

179 BATS (Biosphere–Atmosphere Transfer Model); CLASS (Canadian Land Surface Scheme);  
180 SIMGM (Simple topography-based runoff and Groundwater Model); SIMTOP (Simple  
181 Topography-based hydrological model); SSiB (Simplified Simple Biosphere model).

### 182 2.3 Methods for sensitivity analysis

183 The simulated snow cover events (SCEs) was quantitatively evaluated using the  
184 overall accuracy index (OA) (Toure et al., 2016):

$$185 \quad OA = \frac{a + d}{a + b + c + d}$$

186 where  $a$  is the positive hits,  $b$  represents the false alarm,  $c$  is the misses, and  $d$   
187 represents the negative hits. The value of OA range from 0 to 1. A higher OA signifies  
188 better performance. Ground albedo was used as an indicator for snow events due to a  
189 lack of snow depth observations. The days when the daily mean albedo is greater than  
190 the observed mean value of the warm and cold season (0.25 and 0.30, respectively) are  
191 identified as snow cover.

192 The root mean square error (RMSE) between the simulations and observations  
193 were adopted to evaluate the performance of Noah-MP in simulating soil hydrothermal  
194 dynamics.

195 To investigate the influence degrees of each physical process on SCEs, ST and  
196 SLW, we firstly calculated the mean OA (for SCE) and mean RMSE (for ST and SLW)  
197 ( $\bar{Y}_j^i$ ) of the  $j$ th parameterization schemes ( $j = 1, 2, \dots$ ) in the  $i$ th process ( $i = 1, 2, \dots$ ).

198 Then, the maximum difference of  $\bar{Y}_j^i$  ( $\Delta\bar{OA}$  or  $\Delta\bar{RMSE}$ ) was defined to quantify the  
199 sensitivity of the  $i$ th process ( $i = 1, 2, \dots$ ) (Li et al., 2015):

$$200 \quad \Delta\bar{OA} \text{ or } \Delta\bar{RMSE} = \bar{Y}_{max}^i - \bar{Y}_{min}^i$$

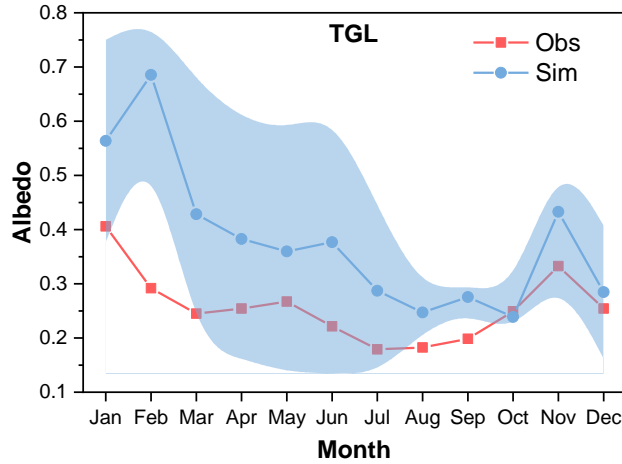
201 where  $\bar{Y}_{max}^i$  and  $\bar{Y}_{min}^i$  are the largest and the smallest  $\bar{Y}_j^i$  in the  $i$ th process,  
202 respectively. For a given physical process, a high  $\Delta\overline{OA}$  or  $\Delta\overline{RMSE}$  signifies large  
203 difference between parameterizations, indicating high sensitiveness of the  $i$ th process  
204 for SCEs and ST/SLW simulation.

205 The sensitivities of physical processes were determined by quantifying the  
206 statistical distinction level of performance between parameterization schemes. The  
207 Independent-sample T-test (2-tailed) was adopted to identify whether the distinction  
208 level between two schemes is significant, and that between three or more schemes was  
209 tested using the Tukey's test. Tukey's test has been widely used for its simple  
210 computation and statistical features (Benjamini, 2010). The detailed descriptions about  
211 this method can be found in Zhang et al. (2016), Gan et al. (2019), and You et al. (2020).  
212 A process can be considered sensitive when the schemes show significant difference.  
213 Moreover, schemes with large mean OA and small mean RMSE were considered  
214 favorable for SCEs and ST/SLW simulation, respectively. We distinguished the  
215 differences of the parameterization schemes at 95% confidence level.

## 216 **3 Results**

### 217 **3.1 General performance of the ensemble simulation**

218 The performance of Noah-MP for snow simulation was firstly tested by conducting  
219 an ensemble of 55296 experiments. Due to a lack of snow depth measurements, ground  
220 albedo was used as an indicator for snow cover. Figure 2 shows the monthly variations  
221 of observed ground albedo and the simulations produced by the ensemble simulations.  
222 The ground albedo was extremely overestimated with large uncertainties when  
223 considering the snow options in Noah-MP, indicating the overestimation of snow depth  
224 and duration. Such overestimation continued till July.



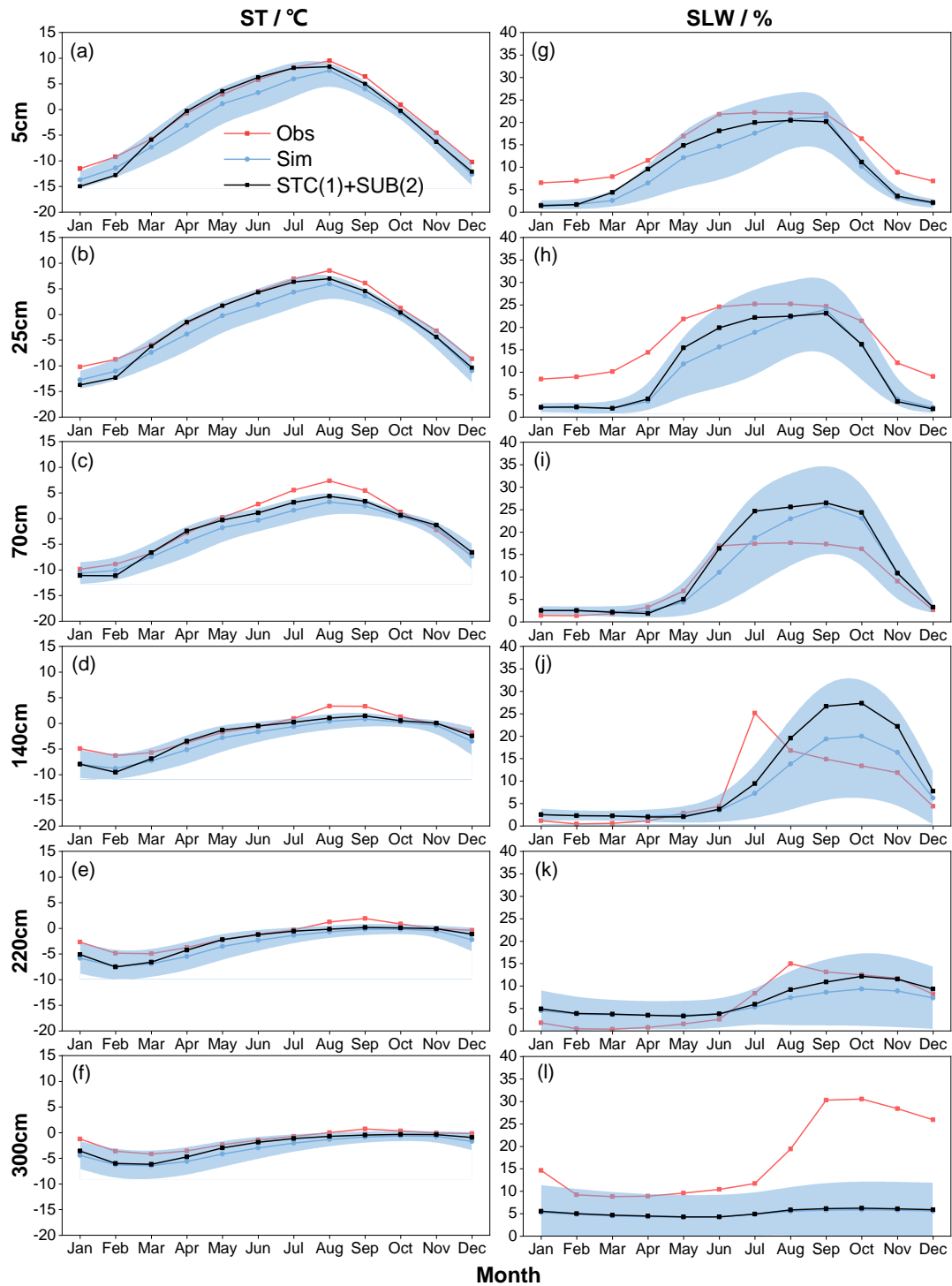
225

226 **Figure 2.** Monthly variations of ground albedo at TGL site for observation (Obs), and  
 227 the ensemble simulation (Sim). The light blue shadow represents the standard deviation  
 228 of the ensemble simulation.

229 Figure 3 illustrates the ensemble simulated and observed annual cycle of ST and  
 230 SLW at TGL site. The ensemble experiments basically captured the seasonal variability  
 231 of ST, whose magnitude decreased with soil depth. In addition, the simulated ST in the  
 232 snow-affected season (October-July) showed relatively wide uncertainty ranges,  
 233 particularly at the shallow layers. This indicates that the selected schemes perform  
 234 much differently for snow simulation, resulting in large uncertainties of shallow STs.  
 235 The simulated ST were generally smaller than the observations with relatively large  
 236 gaps during the snow-affected season. It indicates that the Noah-MP model generally  
 237 underestimates the ST, especially during the snow-affected months.

238 Since the observation equipment can only record the liquid water, soil liquid water  
 239 (SLW) was evaluated against simulations from the ensemble experiments (Fig. 3). The  
 240 Noah-MP model generally underestimated surface (5cm and 25cm) and deep (220cm  
 241 and 300cm) SLW (Fig. 3g, 3h, 3k, 3l). However, Noah-MP tended to overestimate the  
 242 SLW at the middle layers of 70cm and 140cm. Moreover, the simulated SLW exhibited  
 243 relatively wide uncertainty ranges, particularly during the warm season (Fig. 3).

244

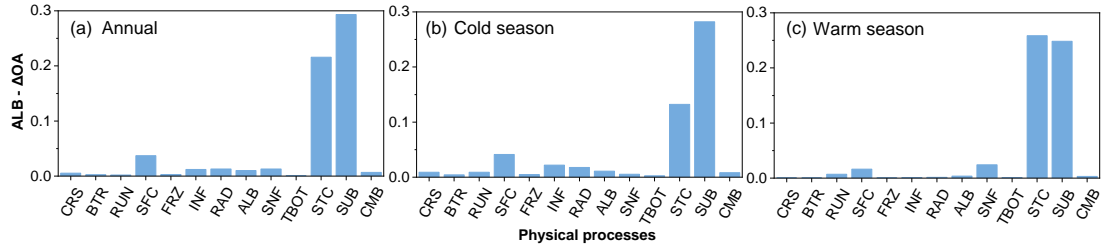


245

246 **Figure 3.** Monthly soil temperature (ST in °C) and soil liquid water (SLW in %) at (a,  
 247 g) 5 cm, (b, h) 25 cm, (c, i) 70 cm, (d, j) 140 cm, (e, k) 220 cm, (f, l) 300 cm at TGL  
 248 site. The light blue shadow represents the standard deviation of the ensemble simulation.  
 249 The black line-symbol represents the ensemble mean of simulations with STC(1) and  
 250 SUB(2).

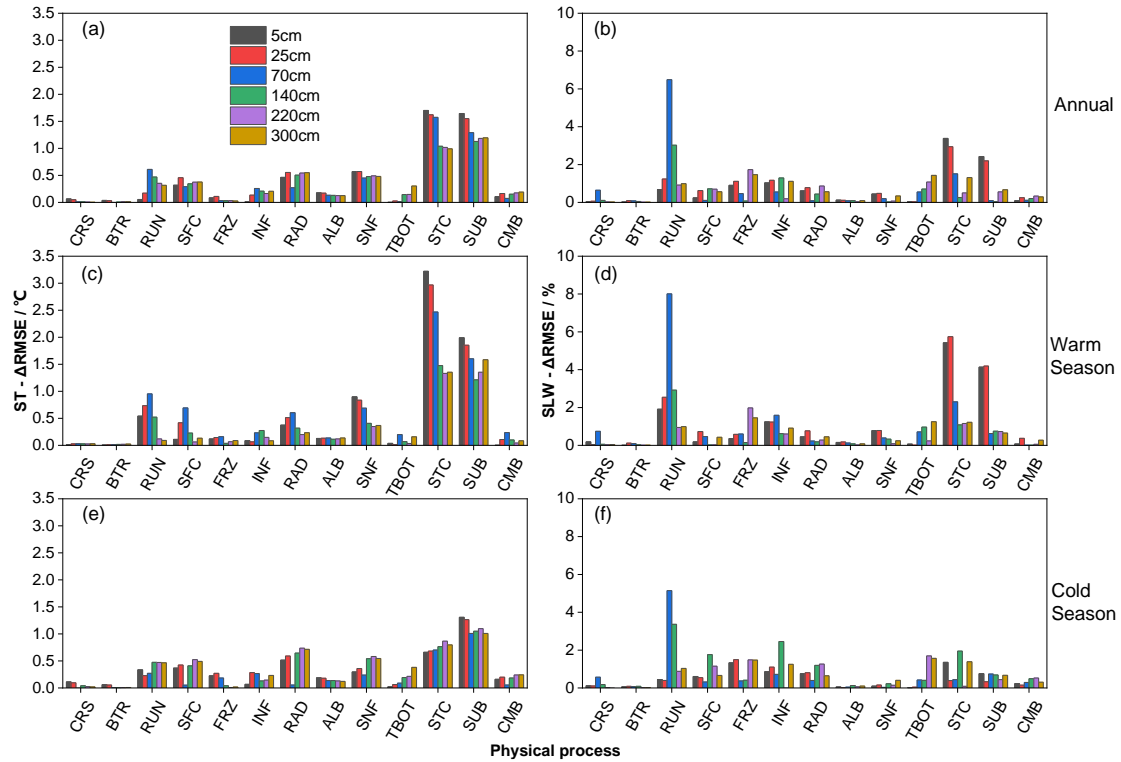
251 **3.2 Sensitivity of physical processes**

252 **3.2.1 Influence degrees of physical processes**



253 **Figure 4.** The maximum difference of the mean overall accuracy (OA) for albedo  
254 (ALB- $\Delta OA$ ) in each physical process during the (a) annual, (b) cold season, and (c)  
255 warm season at TGL site.  
256

257 Figure. 4 compares the influence scores of the 13 physical processes based on the  
258 maximum difference of the mean OA over 55296 experiments using the same scheme,  
259 for SCEs at TGL site. On the whole, the SUB and STC processes had the largest scores  
260 for the whole year as well as during both the warm and cold seasons, and the other  
261 processes showed a value less than 0.05 (Fig. 4a, 4b, 4c). Moreover, the SUB process  
262 had a consistent influence on SCEs while the influence of STC differed with season. In  
263 the cold season, the score of SUB process (0.28) was two times more than that of the  
264 STC process (Fig. 4b), indicating the relative importance of snow sublimation for SCEs  
265 simulation during the cold season. When it comes to the warm season, the influence  
266 score of SUB (0.25) did not change much, while that of STC increased to 0.26 and  
267 showed a similar influence on SCEs simulation with SUB.



268

269 **Figure 5.** The maximum difference of the mean RMSE for (a, c and e) soil temperature  
 270 ( $ST-\overline{\Delta RMSE}$  in  $^{\circ}C$ ) and (b, d and f) soil liquid water ( $SLW-\overline{\Delta RMSE}$  in  $\%$ ) in each  
 271 physical process during the (a and b) annual, (c and d) warm, and (e and f) cold season  
 272 at different soil depths at TGL site.

273 Figure. 5 compares the influence scores of the 13 physical processes at different  
 274 soil depths, based on the maximum difference of the mean RMSE over 55296  
 275 experiments using the same scheme, for ST and SLW at TGL site. The snow-related  
 276 processes, including the STC, SUB and SNF process showed the largest  $ST-\overline{\Delta RMSE}$  at  
 277 all layers, followed by the RAD, SFC and RUN processes. While the  $ST-\overline{\Delta RMSE}$  of  
 278 the other 7 physical processes were less than  $0.5^{\circ}C$ , among which the influence of CRS  
 279 and BTR processes were negligible. What's more, the FRZ, INF, and TBOT processes  
 280 had larger influence scores during the cold season than warm season, and the scores of  
 281 TBOT were greater in deep soils than shallow soils. During the warm season, the  
 282 physical processes generally showed more influence on shallow soil temperatures.  
 283 When it comes to the cold season, the influence of the physical processes on deep layers  
 284 obviously increased and comparable with that on shallow layers, implying the relatively  
 285 higher uncertainties of Noah-MP during the cold season.

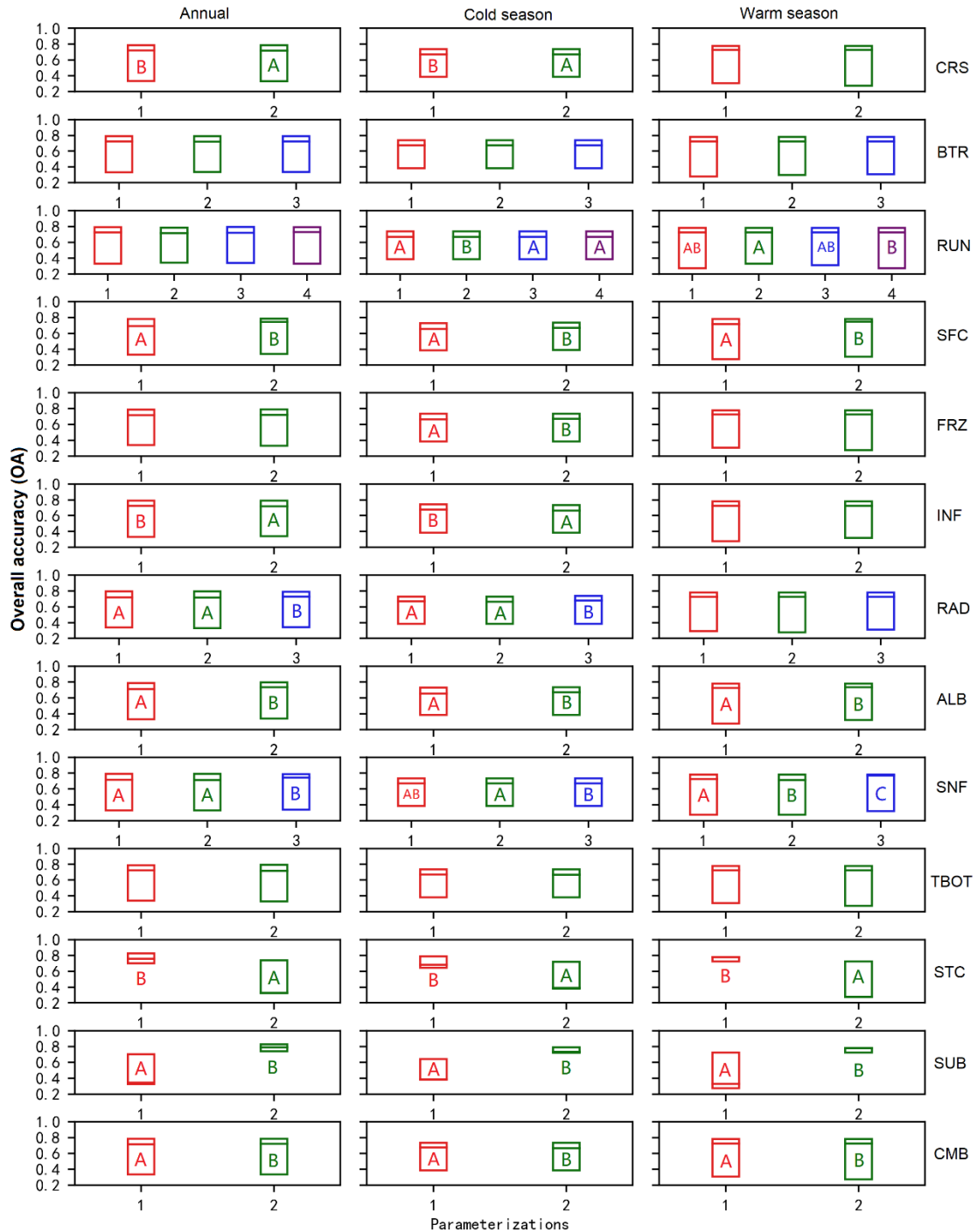
286 Most of the  $\overline{\Delta RMSE}$  for SLW are less than 5%, indicating that all the physical  
287 processes have limited influence on the SLW, among which CRS, BTR, ALB, SNF, and  
288 CMB showed the smallest effects on SLW (Fig. 5b, 5d, 5f). During the warm season,  
289 the RUN process, together with the STC and SUB processes, dominated the  
290 performance of SLW simulation, especially at shallow layers (5cm, 25cm and 70cm,  
291 Fig. 5d). During the cold season, however, the RUN process dominated the SLW  
292 simulation with a great decline of dominance of STC and SUB processes.

### 293 **3.2.2 Sensitivities of physical processes and general behaviors of** 294 **parameterizations**

295 To further investigate the sensitivity of each process and the general performance  
296 of the parameterizations, the Independent-sample T-test (2-tailed) and Tukey's test were  
297 conducted to test whether the difference between parameterizations within a physical  
298 process is significant (Fig. 6 and 7). In a given sub-process, any two schemes labelled  
299 with different letters behave significantly different, and this sub-process therefore can  
300 be identified as sensitive. Otherwise, the sub-process is considered insensitive. For  
301 simplicity, schemes of insensitive sub-process are not labeled. Moreover, schemes with  
302 the letters late in the alphabet have smaller mean RMSEs and outperform the ones with  
303 the letters forward in the alphabet. Using the two schemes in CRS process (hereafter  
304 CRS(1) and CRS(2)) in Fig. 6 as an example. For the annual and warm season, CRS(1)  
305 and CRS(2) were labeled with "B" and "A", respectively. In the cold season, none of  
306 them were labeled with letters. As described above, the CRS process was sensitive for  
307 SCEs simulation during the annual and warm season, and CRS(1) outperformed  
308 CRS(2). However, it was not sensitive during the cold season.

309 Consistent with the influence degrees in Fig. 4, the performance difference  
310 between schemes of the STC and SUB for SCEs simulation were significantly greater  
311 than other processes. Most other physical processes showed significant but limited  
312 difference. Schemes in BTR and TBOT processes, however, had no significant different  
313 performance. Specifically, the performance order followed  $STC(1) > STC(2)$ ,  $SUB(2) >$   
314  $SUB(1)$ ,  $SFC(2) > SFC(1)$ ,  $ALB(2) > ALB(1)$ ,  $CMB(2) > CMB(1)$  in both annual and

315 seasonal scales. RAD showed no obvious difference during the warm season, while  
 316 RAD(3) outperformed RAD(1) and (2) during the cold season. For SNF, SNF(3)  
 317 generally excel SNF(1) and SNF(2), especially during the warm season.



318  
 319 **Figure 6.** Distinction level for overall accuracy (OA) of snow cover events (SCEs)  
 320 during the annual, warm, and cold seasons at TGL site. Limits of the boxes represent  
 321 upper and lower quartiles, lines in the box indicate the median value.

322 All the physical processes showed sensitivities for ST and SLW simulation in

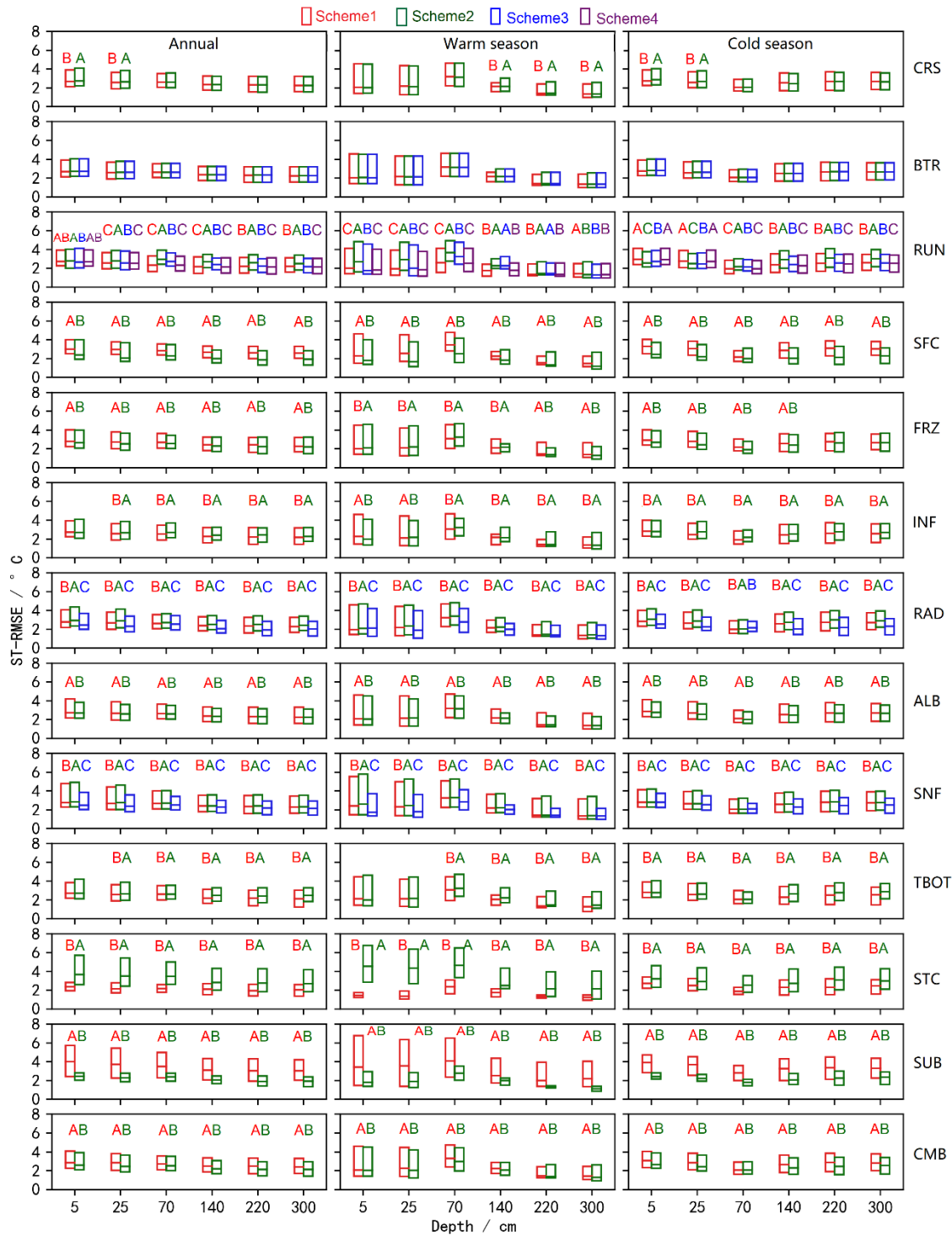


323 varying magnitudes except the BTR process and CRS process in most layers. For ST,  
324 the performance difference between schemes of the STC, SUB and SNF were obviously  
325 greater than other processes, indicating the importance of snow on ST, followed by the  
326 RAD, SFC and RUN processes. The performance orders followed  $STC(1) > STC(2)$ ,  
327  $SUB(2) > SUB(1)$ ,  $SNF(3) > SNF(1) > SNF(2)$ ,  $RAD(3) > RAD(1) > RAD(2)$ , and  
328  $SFC(2) > SFC(1)$ . For SLW, the RUN, STC, and SUB processes showed significant and  
329 higher sensitivities than other physical processes, especially during the warm season  
330 and at the shallow layers (Fig. xx). Consistent with that of ST, the performance orders  
331 for SLW simulation were  $STC(1) > STC(2)$ , and  $SUB(2) > SUB(1)$ . For the RUN  
332 process, the performance orders for both ST and SLW simulation generally followed  
333  $RUN(4) > RUN(1) > RUN(3) > RUN(2)$  as a whole, among which  $RUN(1)$  and  $RUN(4)$   
334 presented similar performance during both warm and cold seasons. During both warm  
335 and cold seasons, the performance orders for ST simulations were  $SFC(2) > SFC(1)$  for  
336 SFC process,  $FRZ(2) > FRZ(1)$  for FRZ process, and  $RAD(3) > RAD(1) > RAD(2)$  for  
337 RAD process (Fig. S2 and S3), which are particularly so for SLW simulations at shallow  
338 and deep layers.

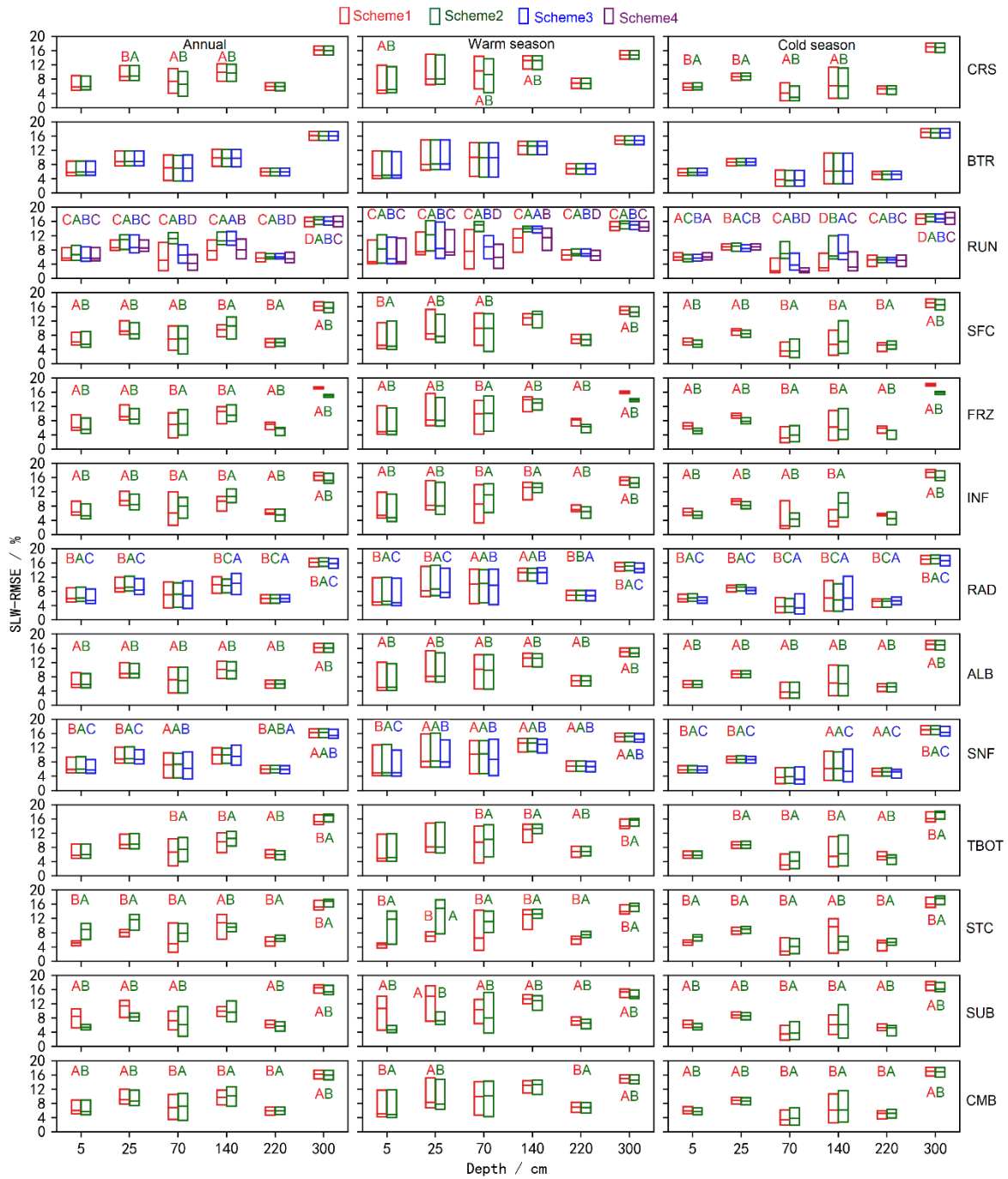
339 For ST, both FRZ and INF showed higher sensitivities during the cold season,  
340 especially at shallow soils for FRZ and deep soils for INF.  $FRZ(2)/INF(1)$  outperformed  
341  $FRZ(1)/INF(2)$  for the whole year for ST simulation. Specifically,  $FRZ(1)/INF(2)$   
342 performed better at the shallow soils during the warm season while did worse during  
343 the cold season compared with  $FRZ(2)/INF(1)$ . For SLW,  $FRZ(2)/INF(2)$  generally  
344 preceded  $FRZ(1)/INF(1)$  at shallow and deep soils (5cm, 25cm, 220cm, and 300cm)  
345 while did worse at middle soil layers (140cm and 220cm).

346 For ST simulation, the performance sequence in RAD and SNF was  $RAD(3) >$   
347  $RAD(1) > RAD(2)$  and  $SNF(3) > SNF(1) > SNF(2)$ , respectively. For SLW simulation,  
348 the sequence become complicated. However,  $RAD(3)$  and  $RAD(3)$  still outperformed  
349 the other two schemes, respectively.  $ALB(2)$  was superior to  $ALB(1)$  for both ST and  
350 SLW simulation. The influence of TBOT on soil hydrothermal arose at deep soils and  
351 during cold season, and  $TBOT(1)$  excel  $TBOT(2)$ .  $CMB(2)$  outperformed  $CMB(1)$  for

352 ST simulation, so did that for SLW simulation at shallow and deep soils (5cm, 25cm,  
 353 and 300cm).



354  
 355 **Figure 7.** Distinction level for RMSE of ST at different layers during the annual, warm,  
 356 and cold seasons in the ensemble simulations at TGL site. Limits of the boxes represent  
 357 upper and lower quartiles, lines in the box indicate the median value.



359

360

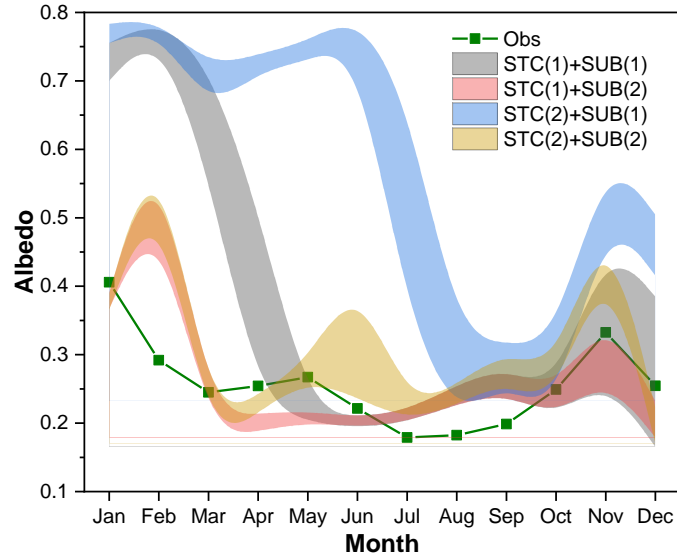
**Figure 8.** Same as in Figure 7 but for SLW.

361

**3.3 Influence of snow cover and surface drag coefficient on soil hydrothermal dynamics**

362

363



364

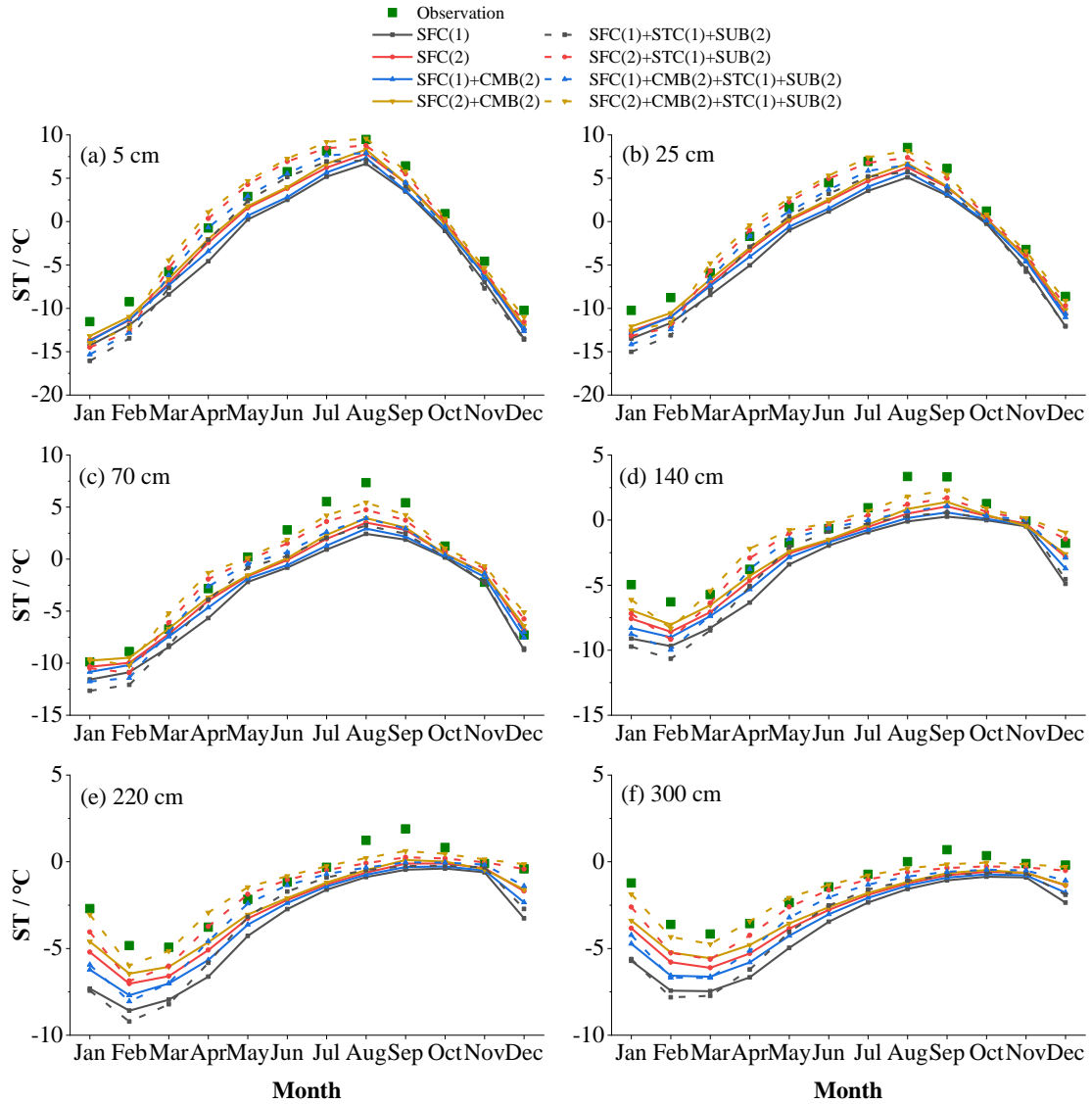
365 **Figure 9.** Uncertainty interval of ground albedo at TGL site in dominant physical  
 366 processes (STC and SUB) for snow cover event simulation.

367 The influence of snow on soil temperature is firstly investigated. The dominant  
 368 role of STC and SUB in the simulation of SCEs has been identified (Fig. 4 and 6).  
 369 Interactions between the two physical processes are further analyzed here. Figure 9  
 370 compares the uncertainly intervals of the two physics. The duration of snow cover is  
 371 the longest when STC(2)+SUB(1), followed when STC(2)+SUB(1). Simulations  
 372 considering SUB(2) generally has a short snow duration. Among the four combinations,  
 373 STC(1)+SUB(2) is in best agreement with the measurements.

374 Given the good performance of STC(1)+SUB(2) in simulating SCEs, the influence  
 375 of snow on soil hydrothermal dynamics is investigated by comparing the total ensemble  
 376 mean ST and SLW with those adopting STC(1)+SUB(2) (Fig. 3). It can be seen that the  
 377 ensemble mean ST of simulations adopting STC(1) and SUB(2) are generally higher  
 378 than the total ensemble means, especially during the spring and summer (Mar.-Aug.).  
 379 In January and February at shallow layers (5cm, 25cm and 70cm), STC(1)+SUB(2) had  
 380 a lower ST and showed an insulation effect on ST during the two months. As a whole,  
 381 however, snow cover has a cooling effect on ST. In addition, along with the improved  
 382 SCEs and elevated ST, STC(1)+SUB(2) induced moister soil with higher SLW (Fig. 3).

383

384



385

386 **Figure 10.** Monthly soil temperature (ST in °C) at (a) 5 cm, (b) 25 cm, (c) 70 cm, (d)  
 387 140 cm, (e) 220 cm, (f) 300 cm for the SFC process that consider the CMB(2) and  
 388 STC(1)+SUB(2) processes or not.

389 SFC and CMB process using different ways to calculate the surface drag  
 390 coefficient, which is of great influence for surface energy partitioning and thus ST and  
 391 SLW. The influence of surface drag coefficient is assessed by comparing the soil  
 392 temperature before and after considering the combined scheme (CMB(2)) and the effect  
 393 of snow (STC(1)+SUB(2)) (Fig. 10). SFC(2) tended to produce higher ST than SFC(1),  
 394 especially during the warming period (January-August). When adopting the combined  
 395 scheme of Y08 and UCT (CMB(2)), the cold bias were significantly resolved. The  
 396 performance order followed  $SFC(2)+CMB(2) > SFC(2) > SFC(1)+CMB(2) > SFC(1)$ .

397 However, considerable underestimations of ST still exist at all layers due to the poor  
398 representation of snow process. After eliminating the effects of snow (STC(1)+SUB(2),  
399 dash lines in Fig. 10), the simulated ST accordingly increased except in January and  
400 February. SFC(2) and SFC(2)+CMB(2) overestimated STs from March to July at  
401 shallow layers (5cm and 25cm), resulting in good agreements of deep STs with  
402 observations. In contrast, the simulated STs at shallow layers (5cm and 25cm) by SFC(1)  
403 and SFC(1)+CMB(2) were basically consistent with observations from March to July.  
404 While large cold bias remained at deep layers.

## 405 **4 Discussion**

### 406 **4.1 Snow cover on the QTP and its influence on soil hydrothermal regime**

407 Snow cover in the permafrost regions of the QTP is thin, patchy, and short-lived  
408 (Che et al., 2019), whose influence on soil temperature and permafrost state is usually  
409 considered weak (Jin et al., 2008; Zou et al., 2017; Wu et al., 2018; Zhang et al., 2018;  
410 Yao et al., 2019). However, our ensemble simulations showed that the surface albedo  
411 is extremely overestimated in both magnitude and duration (Fig. 2), implying an  
412 extreme overestimation of snow cover, which is consistent with the studies using Noah-  
413 MP model (Jiang et al., 2020; Li et al., 2020; Wang et al., 2020) and widely found in  
414 other state-of-the-art LSMs (Wei and Dong, 2015) on the QTP.

415 Great efforts to resolve the overestimation of snow cover in LSMs include  
416 considering the vegetation effect (Park et al., 2016), the snow cover fraction (Jiang et  
417 al., 2020), the blowing snow (Xie et al., 2019), and the fresh snow albedo (Wang et al.  
418 2020). Our results illustrated the superiority of considering the snow sublimation from  
419 wind (SUB(2)) and using semi-implicit snow/soil temperature time scheme (STC(1))  
420 (Fig. 4, 6 and 9) when simulating snow cover on the QTP. It is consistent with previous  
421 conclusions that accounting for the loss resulting from wind contributes to improve  
422 snow cover days and depth (Yuan et al., 2016), and that STC(1) has a rapid snow  
423 ablation than STC(2) (You et al., 2020).

424 The impacts of snow cover on soil temperature in magnitude and vector (cooling or  
425 warming) depend on its timing, duration, and depth (Zhang et al., 2005). In January and  
426 February, the ground heat flux mainly goes upward, the warming effect of simulated  
427 snow can be related to the overestimated snow depth that prevent heat loss from the  
428 ground. During the spring and summer when snow melts, the cooling effects occurs,  
429 mainly because considerable energy that used to heat the ground is reflected due to the  
430 high albedo of snow. With the improvement of snow (STC(1)+SUB(2)), the originally  
431 overestimated snow melts and infiltrated into the soil, resulting in improved SLWs (Fig.  
432 3). And higher soil temperature also contributed to the SLWs according to the freezing-  
433 point depression equation, in which SLW exponentially increase with soil temperature  
434 for a given site (Niu and Yang, 2006).

## 435 **4.2 Discussions on the sensitivity of physical processes on soil hydrothermal** 436 **simulation**

### 437 **4.2.1 Canopy stomatal resistance (CRS) and soil moisture factor for stomatal** 438 **resistance (BTR)**

439 The biophysical process BTR and CRS directly affect the canopy stomatal  
440 resistance and thus the plant transpiration (Niu et al., 2011). The transpiration of plants  
441 could impact the ST/SLW through its cooling effect (Shen et al., 2015) and the water  
442 balance of root zone (Chang et al., 2020). However, the annual transpiration of alpine  
443 steppe is weak due to the shallow effective root zone and lower stomatal control in this  
444 dry environment (Ma et al., 2015), which may explain the indistinctive or very small  
445 difference among the schemes of the BTR and CRS processes for SCEs (Fig. 8), ST  
446 (Fig. 7) and SLW (Fig. 8).

### 447 **4.2.2 Runoff and groundwater (RUN)**

448 In the warm season, different SLWs would result in the difference of the surface  
449 energy partitioning and thus different soil temperatures. RUN(2) had the worst  
450 performance for simulating ST and SLW (Fig. 7 and 8) among the four schemes, likely

451 due to its higher estimation of soil moisture (Fig. S1) and thus greater sensible heat and  
452 smaller ST (Gao et al., 2015). Likewise, RUN(4) was on a par with RUN(1) in the  
453 simulation of ST at most layers due to the very small difference in SLW of two schemes  
454 (Fig. 8 and S1). For the whole soil column, RUN(4) surpassed RUN(1) and RUN(2) for  
455 SLW simulation, both of which define surface/subsurface runoff as functions of  
456 groundwater table depth (Niu et al., 2005; Niu et al., 2007). This is in keeping with the  
457 study of Zheng et al. (2017) that soil water storage-based parameterizations outperform  
458 the groundwater table-based parameterizations in simulating the total runoff in a  
459 seasonally frozen and high-altitude Tibetan river. Besides, RUN(4) is designed based  
460 on the infiltration-excess runoff (Yang and Dickinson, 1996) in spite of the saturation-  
461 excess runoff in RUN(1) and RUN(2) (Gan et al., 2019), which is more common in arid  
462 and semiarid areas like the permafrost regions of QTP (Pilgrim et al., 1988). In the cold  
463 season, much of the liquid water freezes into ice, which would greatly influence the  
464 thermal conductivity of frozen soil considering thermal conductivity of ice is nearly  
465 four times that of the equivalent liquid water. Therefore, the impact of RUN is important  
466 for the soil temperature simulations at both warm and cold seasons (Fig. 5 and 7).

#### 467 **4.2.3 Surface layer drag coefficient (SFC and CMB)**

468 SFC defines the calculations of the surface exchange coefficient for heat and water  
469 vapor (CH), which greatly impact the energy and water balance and thus the  
470 temperature and moisture of soil (Zeng et al., 2012; Zheng et al., 2012). SFC(1) adopts  
471 the Monin-Obukhov similarity theory (MOST) with a general form, while the SFC(2)  
472 uses the improved MOST modified by Chen et al. (1997). In SFC(1), the roughness  
473 length for heat ( $Z_{0h}$ ) is taken as the same with the roughness length for momentum ( $Z_{0m}$ ,  
474 Niu et al., 2011). SFC(2) adopts the Zilitinkevitch approach for  $Z_{0,h}$  calculation  
475 (Zilitinkevich, 1995). The difference between SFC(1) and SFC(2) has a great impact  
476 on the CH value. Several studies have reported that SFC(2) has a better performance  
477 for the simulation of sensible and latent heat on the QTP (Zhang et al., 2016; Gan et al.,  
478 2019). The results of T-test in this study showed remarkable distinctions between the  
479 two schemes, where SFC(2) was dramatically superior to SFC(1) (Fig. 7, and 8). SFC(2)



480 produces lower CH than SFC(1) (Zhang et al., 2014), resulting in less efficient  
481 ventilation and greater heating of the land surface (Yang et al., 2011b), and substantial  
482 improvement of the cold bias of Noah-MP in this study (Fig. 7 and 10).

483 Both SFC(1) and SFC(2) couldn't produce the diurnal variation of Z0,h (Chen et  
484 al., 2010). CMB offers a scheme that considered the diurnal variation of Z0,h in bare  
485 ground and under-canopy turbulent exchange in sparse vegetated surfaces (Li et al.,  
486 2020). Consistent with previous studies in the QTP (Chen et al., 2010; Guo et al., 2011;  
487 Zheng et al., 2015; Li et al., 2020), the simulated ST generally followed  
488  $SFC(2)+CMB(2) > SFC(2) > SFC(1)+CMB(2) > SFC(1)$  with/without removing the  
489 overestimation of snow (Fig. 10), indicating that CMB(2) contributes to resolve the  
490 cold bias of LSMs. However, none of the four combinations could well reproduce the  
491 shallow and deep STs simultaneously. When the snow is well-simulated,  
492 SFC(2)+CMB(2) performed the best at deep layers at the cost of overestimating shallow  
493 STs. Meanwhile, SFC(1)+CMB(1) showed the best agreements at shallow layers with  
494 considerable cold bias at deep layers, which can be related to the overestimated frozen  
495 soil thermal conductivity (Luo et al., 2009; Chen et al., 2012; Li et al., 2019).

#### 496 **4.2.4 Super-cooled liquid water (FRZ) and frozen soil permeability (INF)**

497 FRZ and INF describe the unfrozen water and permeability of frozen soil, and had  
498 a larger influence on ST/SLW during the cold season than warm season as expected  
499 (Fig. 5). Specifically, FRZ treats liquid water in frozen soil (super-cooled liquid water)  
500 using two forms of freezing-point depression equation. FRZ(1) takes a general form  
501 (Niu and Yang, 2006), while FRZ(2) exhibits a variant form that considers the increased  
502 surface area of icy soil particles (Koren et al., 1999). FRZ(2) generally yields more  
503 liquid water in comparison of FRZ(1) (Fig. S2). INF(1) uses soil moisture (Niu and  
504 Yang, 2006) while INF(2) employs only the liquid water (Koren et al., 1999) to  
505 parameterize soil hydraulic properties. INF(2) generally produces more impermeable  
506 frozen soil than INF(1), which is also found in this study (Fig. S3). For the whole year,  
507 INF(1) surpassed INF(2) in simulating STs, which may be related to the more realistic  
508 SLWs produced by INF(1) for the whole soil column (Fig. S3).

#### 509 **4.2.5 Canopy gap for radiation transfer (RAD)**

510 RAD treats the radiation transfer process within the vegetation, and adopts three  
511 methods to calculate the canopy gap. RAD(1) defines canopy gap as a function of the  
512 3D vegetation structure and the solar zenith angle, RAD(2) employs no gap within  
513 canopy, and RAD(3) treat the canopy gap from unity minus the FVEG (Niu and Yang,  
514 2004). The RAD(3) scheme penetrates the most solar radiation to the ground, followed  
515 by the RAD(1) and RAD(2) schemes. As an alpine grassland, there is a relative low  
516 LAI at TGL site, and thus a quite high canopy gap. So, schemes with a larger canopy  
517 gap could realistically reflect the environment. Consequently, the performance  
518 decreased in the order of  $RAD(3) > RAD(1) > RAD(2)$  for ST/SLW simulation.

#### 519 **4.2.6 Snow surface albedo (ALB) and precipitation partition (SNF)**

520 The ALB describe two ways for calculating snow surface albedo, in which the  
521 ALB(1) and ALB(2) adopt the scheme from BATS and CLASS LSM, respectively.  
522 ALB(2) generally produce lower albedo than ALB(1), especially when the ground  
523 covered by snow (Fig. S4). As a result, higher net radiation absorbed by the land surface  
524 and more heat is available for heating the soil in ALB(2), which is beneficial for  
525 counteracting the cooling effect of overestimated snow on ST (Fig. S5). Along with the  
526 higher ST, ALB(2) outperformed ALB(1) for SLW simulation, likely due to more snow  
527 melt water offset the dry bias in Noah-MP (Fig. S5).

528 The SNF defines the snowfall fraction of precipitation as a function of surface air  
529 temperature. SNF(1) is the most complicated of the three schemes, in which the  
530 precipitation is considered rain/snow when the surface air temperature is greater/less  
531 than or equal to 2.5/0.5 °C, otherwise, it is recognized as sleet. While SNF(2) and  
532 SNF(3) simply distinguish rain or snow by judging whether the air temperature is above  
533 2.2 °C and 0 °C or not. The significant difference between three schemes for SCEs  
534 simulation during the warm season is consistent with the large difference of snowfall  
535 fraction in this period (Fig. 6 and S6). SNF(3) is the most rigorous scheme and produce  
536 the minimum amount of snow, followed by SNF(1) and SNF(2) with limited difference  
537 (Fig. S6). This exactly explains superiority of SNF(3) for ST and SLW simulation (Fig.

538 7 and 8).

539 **4.2.7 Lower boundary of soil temperature (TBOT) and snow/soil temperature time**  
540 **scheme (STC)**

541 TBOT process adopts two schemes to describe the soil temperature boundary  
542 conditions. TBOT (1) assumes zero heat flux at the bottom of the model, while TBOT(2)  
543 adopts the soil temperature at the 8 m depth (Yang et al., 2011a). In general, TBOT(1)  
544 is expected to accumulate heat in the deep soil and produce higher ST than TBOT(2).  
545 In this study, the two assumptions performed significantly different, especially at the  
546 deep soils and during the cold season. Although TBOT(2) is more representative of the  
547 realistic condition, TBOT(1) surpassed TBOT(2) in this study. It can be related to the  
548 overall underestimation of the model, which can be alleviated by TBOT(1) because of  
549 heat accumulation (Fig. S7).

550 Two time discretization strategies are implemented in the STC process, where  
551 STC(1) adopts the semi-implicit scheme while STC(2) uses the full implicit scheme, to  
552 solve the thermal diffusion equation in first soil or snow layers (Yang et al., 2011a).  
553 STC(1) and STC(2) are not strictly a physical processes but different upper boundary  
554 conditions of soil column (You et al., 2019). The differences between STC(1) and  
555 STC(2) were significant (Fig. 7). The impacts of the two options on ST is remarkable  
556 (Fig. 6), particularly in the shallow layers and during the warm season (Fig. 5). In  
557 addition, STC(1) outperformed STC(2) in the ensemble simulated ST(Fig. 7), because  
558 STC(1) greatly alleviated the cold bias in Noah-MP (Fig. S8) by producing the higher  
559 OA of SCEs (Fig. 6)

560 **4.3 Perspectives**

561 This study analyzed the characteristics and general behaviors of each  
562 parameterization scheme of Noah-MP at a typical permafrost site on the QTP, hoping  
563 to provide a reference for simulating permafrost state on the QTP. We identified the  
564 systematic overestimation of snow cover, cold bias and dry bias in Noah-MP, and

565 discussed the role of snow and surface drag coefficient on soil hydrothermal dynamics.  
566 Relevant results and methodologies can be practical guidelines for improving the  
567 parameterizations of physical processes and testing their uncertainties towards near-  
568 surface permafrost modeling on the plateau. Although the site we selected may be  
569 representative for the typical environment on the plateau, continued investigation with  
570 a broad spectrum of climate and environmental conditions is required to make a general  
571 conclusion at regional scale.

## 572 **5 Conclusions**

573 An ensemble simulation using multi-parameterizations was conducted using the  
574 Noah-MP model at the TGL site, aiming to present a reference for simulating soil  
575 hydrothermal dynamics in the permafrost regions of QTP using LSMs. The model was  
576 modified to consider the vertical heterogeneity in the soil and the simulation depth was  
577 extended to cover the whole active layer. The ensemble simulation consists of 55296  
578 experiments, combining thirteen physical processes (CRS, BTR, RUN, SFC, FRZ, INF,  
579 RAD, ALB, SNF, TBOT, STC, SUB, and CMB) each with multiple optional schemes.  
580 On this basis, the general performance of Noah-MP was assessed by comparing  
581 simulation results with in situ observations, and the sensitivity of snow cover event, soil  
582 temperature and moisture at different depths of active layer to parameterization  
583 schemes was explored. The main conclusions are as follows:

- 584 (1) Noah-MP model tends to overestimate snow cover, which is most influenced by the  
585 STC and SUB processes. Such overestimation can be greatly resolved by  
586 considering the snow sublimation from wind (SUB(2)) and semi-implicit snow/soil  
587 temperature time scheme (STC(1)).
- 588 (2) Soil temperature is largely underestimated by the overestimated snow cover and  
589 thus dominated by the STC and SUB processes. Systematic cold bias and large  
590 uncertainties of soil temperature still exist after eliminating the effects of snow,  
591 particularly at the deep layers and during the cold season. The combination of Y08  
592 and UCT contributes to resolve the cold bias of soil temperature.

593 (3) Noah-MP tend to underestimate soil liquid water content. Most physical processes  
594 have limited influence on soil liquid water content, among which the RUN process  
595 plays a dominant role during the whole year. The STC and SUB process have a  
596 considerable influence on topsoil liquid water during the warm season.

597

598 *Code availability.* The source code of offline 1D Noah-MP LSM v1.1 is available at  
599 [https://ral.ucar.edu/solutions/products/noah-multiparameterization-land-surface-](https://ral.ucar.edu/solutions/products/noah-multiparameterization-land-surface-model-noah-mp-lsm)  
600 [model-noah-mp-lsm](https://ral.ucar.edu/solutions/products/noah-multiparameterization-land-surface-model-noah-mp-lsm) (last access: 15 May 2020). The modified Noah-MP with the  
601 consideration of vertical heterogeneity, extended soil depth, and pedotransfer functions  
602 is available upon request to the corresponding author. The data processing code are  
603 available at <http://dx.doi.org/10.17632/gc7vfgkyng.1>.

604

605 *Data availability.* The 1-hourly forcing data and daily soil temperature data at the TGL  
606 site are available at <http://dx.doi.org/10.17632/gc7vfgkyng.1>. Soil texture data can be  
607 obtained at <https://doi.org/10.1016/j.catena.2017.04.011> (Hu et al., 2017). The AVHRR  
608 LAI data can be downloaded from <https://www.ncei.noaa.gov/data/> (Claverie et al.,  
609 2016).

610

611 *Author contributions.* TW and XL conceived the idea and designed the model  
612 experiments. XL performed the simulations, analyzed the output, and wrote the paper.  
613 JC helped to compile the model in a Linux environment. XW, XZ, GH, RL contributed  
614 to the conduction of the simulation and interpretation of the results. YQ provided the  
615 observations of atmospheric forcing and soil temperature. CY and JH helped in  
616 downloading and processing the AVHRR LAI data. JN and WM provide guidelines for  
617 the visualization. Everyone revised and polished the paper.

618

619 *Competing interests.* The authors declare that they have no conflict of interest.

620

621 *Acknowledgements.* This work has been supported by the CAS "Light of West China"  
622 Program, and the National Natural Science Foundation of China (41690142; 41771076;

623 41961144021; 41671070). The authors thank Cryosphere Research Station on the  
624 Qinghai-Tibet Plateau, CAS for providing field observation data used in this study. We  
625 would like to thank two anonymous reviewers for their insightful and constructive  
626 comments and suggestions, which greatly improved the quality of the manuscript.

## 627 **References**

- 628 Benjamini, Y.: Simultaneous and selective inference: Current successes and future challenges,  
629 *Biometrical J.*, 52, 708-721, <https://doi.org/10.1002/bimj.200900299>, 2010.
- 630 Cao, B., Zhang, T., Wu, Q., Sheng, Y., Zhao, L., and Zou, D.: Brief communication: Evaluation and  
631 inter-comparisons of Qinghai–Tibet Plateau permafrost maps based on a new inventory of field  
632 evidence, *The Cryosphere*, 13, 511-519, <https://doi.org/10.5194/tc-13-511-2019>, 2019.
- 633 Chang, M., Liao, W., Wang, X., Zhang, Q., Chen, W., Wu, Z., and Hu, Z.: An optimal ensemble of  
634 the Noah-MP land surface model for simulating surface heat fluxes over a typical subtropical  
635 forest in South China, *Agric. For. Meteorol.*, 281, 107815,  
636 <https://doi.org/https://doi.org/10.1016/j.agrformet.2019.107815>, 2020.
- 637 Che, T., Hao, X., Dai, L., Li, H., Huang, X., and Xiao, L.: Snow cover variation and its impacts over  
638 the Qinghai-Tibet Plateau, *Bull. Chin. Acad. Sci.*, 34, 1247-1253,  
639 <https://doi.org/10.16418/j.issn.1000-3045.2019.11.007>, 2019.
- 640 Chen, F., Janjić, Z., and Mitchell, K.: Impact of atmospheric surface-layer parameterizations in the  
641 new land-surface scheme of the NCEP Mesoscale Eta Model. *Boundary-Layer Meteorol.* 85, 391-  
642 421, <https://doi.org/10.1023/A:1000531001463>, 1997.
- 643 Chen, R., Yang, M., Wang, X., and Wan, G.: Review on simulation of land-surface processes on the  
644 Tibetan Plateau, *Sci. Cold Arid Reg.*, 11, 93-115, <https://doi.org/10.3724/SP.J.1226.2019.00093>,  
645 2019.
- 646 Chen, S., Li, X., Wu, T., Xue, K., Luo, D., Wang, X., Wu, Q., Kang, S., Zhou, H., and Wei, D.: Soil  
647 thermal regime alteration under experimental warming in permafrost regions of the central  
648 Tibetan Plateau, *Geoderma*, 372, 114397,  
649 <https://doi.org/https://doi.org/10.1016/j.geoderma.2020.114397>, 2020.
- 650 Chen, Y., Yang, K., Zhou, D., Qin, J., and Guo, X.: Improving the Noah land surface model in arid  
651 regions with an appropriate parameterization of the thermal roughness length, *J. Hydrometeorol.*,  
652 11, 995-1006, <https://doi.org/10.1175/2010JHM1185.1>, 2010.
- 653 Chen, Y., Yang, K., Tang, W., Qin, J., and Zhao, L.: Parameterizing soil organic carbon's impacts  
654 on soil porosity and thermal parameters for Eastern Tibet grasslands, *Sci. Chin. Earth Sci.*, 55,  
655 1001-1011, <https://doi.org/10.1007/s11430-012-4433-0>, 2012.
- 656 Claverie, M., Matthews, J. L., Vermote, E. F., and Justice, C. O.: A 30+ year AVHRR LAI and  
657 FAPAR climate data record: Algorithm description and validation, *Remote Sens.*, 8, 263,  
658 <https://doi.org/10.3390/rs8030263>, 2016.
- 659 Cosby, B. J., Hornberger, G. M., Clapp, R. B., and Ginn, T. R.: A statistical exploration of the  
660 relationships of soil moisture characteristics to the physical properties of soils, *Water Resour. Res.*,  
661 20, 682-690, <https://doi.org/10.1029/WR020i006p00682>, 1984.

662 Daniel, R., Nikolay, S., Bernd, E., Stephan, G., and Sergei, M.: Recent advances in permafrost  
663 modelling, *Permafrost Periglacial Processes*, 19, 137-156, <https://doi.org/doi:10.1002/ppp.615>, 2008.

664 Fountain, A. G., Campbell, J. L., Schuur, E. A. G., Stammerjohn, S. E., Williams, M. W., and  
665 Ducklow, H. W.: The disappearing cryosphere: Impacts and ecosystem responses to rapid  
666 cryosphere loss, *BioScience*, 62, 405-415, <https://doi.org/10.1525/bio.2012.62.4.11>, 2012.

667 Gan, Y. J., Liang, X. Z., Duan, Q. Y., Chen, F., Li, J. D., and Zhang, Y.: Assessment and reduction  
668 of the physical parameterization uncertainty for Noah-MP land surface model, *Water Resour. Res.*,  
669 55, 5518-5538, <https://doi.org/10.1029/2019wr024814>, 2019.

670 Gao, Y., Kai, L., Fei, C., Jiang, Y., and Lu, C.: Assessing and improving Noah-MP land model  
671 simulations for the central Tibetan Plateau, *J. Geophys. Res.-Atmos.*, 120, 9258-9278,  
672 <https://doi.org/10.1002/2015JD023404>, 2015.

673 Guo, D., and Wang, H.: Simulation of permafrost and seasonally frozen ground conditions on the  
674 Tibetan Plateau, 1981-2010, *J. Geophys. Res.-Atmos.*, 118, 5216-5230,  
675 <https://doi.org/10.1002/jgrd.50457>, 2013.

676 Guo, X., Yang, K., Zhao, L., Yang, W., Li, S., Zhu, M., Yao, T., and Chen, Y.: Critical evaluation of  
677 scalar roughness length parametrizations over a melting valley glacier, *Boundary-Layer  
678 Meteorol.*, 139(2), 307-332, <https://doi.org/10.1007/s10546-010-9586-9>, 2011.

679 He, K., Sun, J., and Chen, Q.: Response of climate and soil texture to net primary productivity and  
680 precipitation-use efficiency in the Tibetan Plateau, *Pratacultural Science*, 36, 1053-1065.  
681 <https://doi.org/10.11829/j.issn.1001-0629.2019-0036>, 2019.

682 Hillel, D.: *Applications of Soil Physics*, Academic Press, 400 pp., 1980.

683 Hjort, J., Karjalainen, O., Aalto, J., Westermann, S., Romanovsky, V. E., Nelson, F. E., Etzelmüller,  
684 B., and Luoto, M.: Degrading permafrost puts Arctic infrastructure at risk by mid-century, *Nat.  
685 Commun.*, 9, 5147, <https://doi.org/10.1038/s41467-018-07557-4>, 2018.

686 Hong, S., Yu, X., Park, S. K., Choi, Y. S., and Myoung, B.: Assessing optimal set of implemented  
687 physical parameterization schemes in a multi-physics land surface model using genetic algorithm,  
688 *Geosci. Model Dev.*, 7, 2517-2529, <https://doi.org/10.5194/gmd-7-2517-2014>, 2014.

689 Hu, G., Zhao, L., Li, R., Wu, T., Wu, X., Pang, Q., Xiao, Y., Qiao, Y., and Shi, J.: Modeling  
690 hydrothermal transfer processes in permafrost regions of Qinghai-Tibet Plateau in China, *Chin.  
691 Geograph. Sci.*, 25, 713-727, <https://doi.org/10.1007/s11769-015-0733-6>, 2015.

692 Hu, G., Zhao, L., Wu, X., Li, R., Wu, T., Xie, C., Pang, Q., and Zou, D.: Comparison of the thermal  
693 conductivity parameterizations for a freeze-thaw algorithm with a multi-layered soil in permafrost  
694 regions, *Catena*, 156, 244-251, <https://doi.org/10.1016/j.catena.2017.04.011>, 2017.

695 Jiang, Y., Chen, F., Gao, Y., He, C., Barlage, M., and Huang, W.: Assessment of uncertainty sources  
696 in snow cover simulation in the Tibetan Plateau, *J. Geophys. Res.-Atmos.*, 125, e2020JD032674,  
697 <https://doi.org/10.1029/2020JD032674>, 2020.

698 Jin, H., Sun, L., Wang, S., He, R., Lu, L., and Yu, S.: Dual influences of local environmental  
699 variables on ground temperatures on the interior-eastern Qinghai-Tibet Plateau (I): vegetation and  
700 snow cover. *J. Glaciol. Geocryol.* 30, 535-545, 2008.

701 Koren, V., Schaake, J., Mitchell, K., Duan, Q. Y., Chen, F., and Baker, J. M.: A parameterization of  
702 snowpack and frozen ground intended for NCEP weather and climate models, *J. Geophys. Res.-  
703 Atmos.*, 104, 19569-19585, <https://doi.org/10.1029/1999JD900232>, 1999.

704 Koven, C., Riley, W., and Stern, A.: Analysis of permafrost thermal dynamics and response to  
705 climate change in the CMIP5 earth system models, *J. Clim.*, 26, 1877-1900,

706 <https://doi.org/10.1175/JCLI-D-12-00228.1>, 2013.

707 Lawrence, D., Fisher, R., Koven, C., Oleson, K., Swenson, S., Vertenstein, M.: Technical description  
708 of version 5.0 of the Community Land Model (CLM), Boulder, Colorado, 2018.

709 Li, K., Gao, Y., Fei, C., Xu, J., Jiang, Y., Xiao, L., Li, R., and Pan, Y.: Simulation of impact of roots  
710 on soil moisture and surface fluxes over central Qinghai – Xizang Plateau. *Plateau Meteor.*, 34,  
711 642-652, <https://doi.org/10.7522/j.issn.1000-0534.2015.00035>, 2015.

712 Li, R., Zhao, L., Wu, T., Wang, Q. X., Ding, Y., Yao, J., Wu, X., Hu, G., Xiao, Y., Du, Y., Zhu, X.,  
713 Qin, Y., Shuhua, Y., Bai, R., Erji, D., Liu, G., Zou, D., Yongping, Q., and Shi, J.: Soil thermal  
714 conductivity and its influencing factors at the Tanggula permafrost region on the Qinghai–Tibet  
715 Plateau, *Agric. For. Meteor.*, 264, 235-246, <https://doi.org/10.1016/j.agrformet.2018.10.011>,  
716 2019.

717 Li, X., Wu, T., Zhu, X., Jiang, Y., Hu, G., Hao, J., Ni, J., Li, R., Qiao, Y., Yang, C., Ma, W., Wen, A.,  
718 and Ying, X.: Improving the Noah-MP Model for simulating hydrothermal regime of the active  
719 layer in the permafrost regions of the Qinghai-Tibet Plateau, *J. Geophys. Res.-Atmos.*, 125,  
720 e2020JD032588, <https://doi.org/10.1029/2020JD032588>, 2020.

721 Luo, D., Wu, Q., Jin, H., Marchenko, S., Lyu, L., and Gao, S.: Recent changes in the active layer  
722 thickness across the northern hemisphere, *Environ. Earth Sci.*, 75, 555.  
723 <https://doi.org/10.1007/s12665-015-5229-2>, 2016.

724 Luo, S., Lyu, S., Zhang, Y., Hu, Z., Ma, Y. M., Li, S. S., and Shang, L.: Soil thermal conductivity  
725 parameterization establishment and application in numerical model of central Tibetan Plateau,  
726 *Chin. J. Geophys.*, 52, 919-928, <https://doi.org/10.3969/j.issn.0001-5733.2009.04.008>, 2009.

727 Luo, S., Wang, J., Pomeroy, J. W., and Lyu, S.: Freeze–thaw changes of seasonally frozen ground  
728 on the Tibetan Plateau from 1960 to 2014, *J. Clim.*, 33(21), 9427-9446,  
729 <https://doi.org/10.1175/JCLI-D-19-0923.1>, 2020.

730 Ma, N., Zhang, Y., Guo, Y., Gao, H., Zhang, H., and Wang, Y.: Environmental and biophysical  
731 controls on the evapotranspiration over the highest alpine steppe, *J. Hydrol.*, 529, 980-992,  
732 <https://doi.org/https://doi.org/10.1016/j.jhydrol.2015.09.013>, 2015.

733 Maheu, A., Anctil, F., Gaborit, É., Fortin, V., Nadeau, D. F., and Therrien, R.: A field evaluation of  
734 soil moisture modelling with the Soil, Vegetation, and Snow (SVS) land surface model using  
735 evapotranspiration observations as forcing data, *J. Hydrol.*, 558, 532-545,  
736 <https://doi.org/https://doi.org/10.1016/j.jhydrol.2018.01.065>, 2018.

737 Melton, J., Verseghy, D., Sospedra-Alfonso, R., and Gruber, S.: Improving permafrost physics in  
738 the coupled Canadian Land Surface Scheme (v.3.6.2) and Canadian Terrestrial Ecosystem Model  
739 (v.2.1) (CLASS-CTEM), *Geosci. Model Dev.*, 12, 4443-4467, <https://doi.org/10.5194/gmd-12-4443-2019>, 2019.

741 Nicolsky, D. J., Romanovsky, V. E., Alexeev, V. A., and Lawrence, D. M.: Improved modeling of  
742 permafrost dynamics in a GCM land-surface scheme, *Geophys. Res. Lett.*, 34, L08501,  
743 <https://doi.org/10.1029/2007gl029525>, 2007.

744 Niu, G.-Y., and Yang, Z.-L.: Effects of vegetation canopy processes on snow surface energy and  
745 mass balances, *J. Geophys. Res.-Atmos.*, 109, D23111, <https://doi.org/10.1029/2004jd004884>,  
746 2004.

747 Niu, G.-Y., and Yang, Z.-L.: Effects of frozen soil on snowmelt runoff and soil water storage at a  
748 continental scale, *J. Hydrometeor.*, 7, 937-952, <https://doi.org/10.1175/JHM538.1>, 2006.

749 Niu, G.-Y., Yang, Z.-L., Dickinson, R. E., and Gulden, L. E.: A simple TOPMODEL-based runoff



750 parameterization (SIMTOP) for use in global climate models, *J. Geophys. Res.-Atmos.*, 110,  
751 D21106, <https://doi.org/10.1029/2005jd006111>, 2005.

752 Niu, G.-Y., Yang, Z.-L., Dickinson, R. E., Gulden, L. E., and Su, H.: Development of a simple  
753 groundwater model for use in climate models and evaluation with Gravity Recovery and Climate  
754 Experiment data, *J. Geophys. Res.-Atmos.*, 112, D07103, <https://doi.org/10.1029/2006jd007522>,  
755 2007.

756 Niu, G.-Y., Yang, Z.-L., Mitchell, K. E., Chen, F., Ek, M. B., Barlage, M., Kumar, A., Manning, K.,  
757 Niyogi, D., and Rosero, E.: The community Noah land surface model with multiparameterization  
758 options (Noah-MP): 1. Model description and evaluation with local-scale measurements, *J.*  
759 *Geophys. Res.-Atmos.*, 116, D12109, <https://doi.org/10.1029/2010JD015139>, 2011.

760 Park, S., and Park, S.K.: Parameterization of the snow-covered surface albedo in the Noah-MP  
761 Version 1.0 by implementing vegetation effects, *Geosci. Model Dev.* 9, 1073-1085,  
762 <https://doi.org/10.5194/gmd-9-1073-2016>, 2016.

763 Pilgrim, D. H., Chapman, T. G., and Doran, D. G.: Problems of rainfall-runoff modelling in arid and  
764 semiarid regions, *Hydrolog. Sci. J.*, 33, 379-400, <https://doi.org/10.1080/02626668809491261>,  
765 1988.

766 Qin, Y., Wu, T., Zhao, L., Wu, X., Li, R., Xie, C., Pang, Q., Hu, G., Qiao, Y., Zhao, G., Liu, G., Zhu,  
767 X., and Hao, J.: Numerical modeling of the active layer thickness and permafrost thermal state  
768 across Qinghai-Tibetan Plateau. *J. Geophys. Res.-Atmos.*, 122, 11,604-611,620,  
769 <https://doi.org/10.1002/2017JD026858>, 2017.

770 Schaake, J. C., Koren, V. I., Duan, Q. Y., Mitchell, K., and Chen, F.: Simple water balance model  
771 for estimating runoff at different spatial and temporal scales, *J. Geophys. Res.-Atmos.*, 101, 7461-  
772 7475, <https://doi.org/10.1029/95jd02892>, 1996.

773 Shen, M., Piao, S., Jeong, S.-J., Zhou, L., Zeng, Z., Ciais, P., Chen, D., Huang, M., Jin, C.-S., Li, L.  
774 Z. X., Li, Y., Myneni, R. B., Yang, K., Zhang, G., Zhang, Y., and Yao, T.: Evaporative cooling  
775 over the Tibetan Plateau induced by vegetation growth, *Proc. Natl. Acad. Sci. U. S. A.*, 112, 9299-  
776 9304, <https://doi.org/10.1073/pnas.1504418112>, 2015.

777 Toure, A., Rodell, M., Yang, Z., Beaudoin, H., Kim, E., Zhang, Y., and Kwon, Y.: Evaluation of  
778 the snow simulations from the community land model, version 4 (CLM4). *J. Hydrometeor.*, 17,  
779 153–170, <https://doi.org/10.1175/JHM-D-14-0165.1>, 2016.

780 Wang, X., Chen, R., Han, C., Yang, Y., Liu, J., Liu, Z., Guo, S., and Song, Y.: Response of shallow  
781 soil temperature to climate change on the Qinghai–Tibetan Plateau, *Int. J. Climatol.*, 41, 1-16,  
782 <https://doi.org/10.1002/joc.6605>, 2021.

783 Wang, W., Yang, K., Zhao, L., Zheng, Z., Lu, H., Mamtimin, A., Ding, B., Li, X., Zhao, L., Li, H.,  
784 Che, T., and Moore, J. C.: Characterizing surface albedo of shallow fresh snow and its importance  
785 for snow ablation on the interior of the Tibetan Plateau, *J. Hydrometeor.*, 21, 815-827,  
786 <https://doi.org/10.1175/JHM-D-19-0193.1>, 2020.

787 Wei, Z., and Dong, W.: Assessment of simulations of snow depth in the Qinghai-Tibetan Plateau  
788 using CMIP5 multi-models, *Arct. Antarct. Alp. Res.*, 47, 611-525,  
789 <https://doi.org/10.1657/AAAR0014-050>, 2015.

790 Westermann, S., Langer, M., Boike, J., Heikenfeld, M., Peter, M., Eitzelmüller, B., and Krinner, G.:  
791 Simulating the thermal regime and thaw processes of ice-rich permafrost ground with the land-  
792 surface model CryoGrid 3, *Geosci. Model Dev.*, 9, 523-546, [https://doi.org/10.5194/gmd-9-523-  
793 2016](https://doi.org/10.5194/gmd-9-523-2016), 2016.

794 Wetzel, P., and Chang, J.-T.: Concerning the relationship between evapotranspiration and soil  
795 moisture, *J. Clim. Appl. Meteorol.*, 26, 18-27, <https://doi.org/10.1175/1520->  
796 0450(1987)026<0018:CTRBEA>2.0.CO;2, 1987.

797 Woo, M. K.: *Permafrost Hydrology*, Springer, Berlin, Heidelberg, 2012.

798 Wu, X., and Nan, Z.: A multilayer soil texture dataset for permafrost modeling over Qinghai-Tibetan  
799 Plateau. Paper presented at 2016 IEEE International Geoscience and Remote Sensing Symposium  
800 (IGARSS), Beijing, China. <https://doi.org/10.1109/IGARSS.2016.7730283>, 2016.

801 Wu, X. B., Nan, Z. T., Zhao, S. P., Zhao, L., and Cheng, G. D.: Spatial modeling of permafrost  
802 distribution and properties on the Qinghai-Tibet Plateau, *Permafr. Periglac. Process.*, 29, 86-99,  
803 <https://doi.org/10.1002/ppp.1971>, 2018.

804 Xie, Z., Hu, Z., Ma, Y., Sun, G., Gu, L., Liu, S., Wang, Y., Zheng, H., and Ma, W.: Modeling blowing  
805 snow over the Tibetan Plateau with the community land model: Method and preliminary  
806 evaluation, *J. Geophys. Res.-Atmos.*, 124, 9332–9355, <https://doi.org/10.1029/2019jd030684>,  
807 2019.

808 Yang, K., Koike, T., Ye, B., and Bastidas, L.: Inverse analysis of the role of soil vertical  
809 heterogeneity in controlling surface soil state and energy partition, *J. Geophys. Res.-Atmos.*, 110,  
810 D08101, <https://doi.org/10.1029/2004jd005500>, 2005.

811 Yang, K., Koike, T., Ishikawa, H., Kim, J., Li, X., Liu, H., Shaomin, L., Ma, Y., and Wang, J.:  
812 Turbulent flux transfer over bare-soil surfaces: Characteristics and parameterization, *J. Appl.*  
813 *Meteorol. Clim.*, 47, 276-290, <https://doi.org/10.1175/2007JAMC1547.1>, 2008.

814 Yang, Z.-L., and Dickinson, R. E.: Description of the biosphere-atmosphere transfer scheme (BATS)  
815 for the soil moisture workshop and evaluation of its performance, *Global Planet. Change*, 13,  
816 117-134, [https://doi.org/10.1016/0921-8181\(95\)00041-0](https://doi.org/10.1016/0921-8181(95)00041-0), 1996.

817 Yang, Z.-L., Cai, X., Zhang, G., Tavakoly, A., Jin, Q., Meyer, L., and Guan, X.: The Community  
818 Noah Land Surface Model with Multi-Parameterization Options (Noah-MP): Technical  
819 Description, 2011a.

820 Yang, Z.-L., Niu, G.-Y., E. Mitchell, K., Chen, F., B. Ek, M., Barlage, M., Longuevergne, L.,  
821 Manning, K., Niyogi, D., Tewari, M., and Xia, Y.: The community Noah land surface model with  
822 multiparameterization options (Noah-MP): 2. Evaluation over global river basins. *J. Geophys.*  
823 *Res.-Atmos.* 116, D12110, <https://doi.org/10.1029/2010JD015140>, 2011b.

824 Yao, C., Lyu, S., Wang, T., Wang, J., and Ma, C.: Analysis on freezing-thawing characteristics of  
825 soil in high and low snowfall years in source region of the Yellow River, *Plateau Meteor.*, 38,  
826 474-483, 2019.

827 Yao, J., Zhao, L., Gu, L., Qiao, Y., and Jiao, K.: The surface energy budget in the permafrost region  
828 of the Tibetan Plateau, *Atmos. Res.*, 102, 394-407,  
829 <https://doi.org/https://doi.org/10.1016/j.atmosres.2011.09.001>, 2011.

830 Yi, S., Zhou, Z., Ren, S., Ming, X., Yu, Q., Shengyun, C., and Baisheng, Y.: Effects of permafrost  
831 degradation on alpine grassland in a semi-arid basin on the Qinghai–Tibetan Plateau, *Environ.*  
832 *Res. Lett.*, 6, 045403, <https://doi.org/10.1088/1748-9326/6/4/045403>, 2011.

833 You, Y., Huang, C., Gu, J., Li, H., Hao, X., and Hou, J.: Assessing snow simulation performance of  
834 typical combination schemes within Noah-MP in northern Xinjiang, China, *J. Hydro.*, 581,  
835 124380, <https://doi.org/10.1016/j.jhydrol.2019.124380>, 2020.

836 You, Y., Huang, C., Yang, Z., Zhang, Y., Bai, Y., and Gu, J.: Assessing Noah-MP parameterization  
837 sensitivity and uncertainty interval across snow climates, *J. Geophys. Res.-Atmos.*, 125,

838 e2019JD030417, <https://doi.org/10.1029/2019jd030417>, 2020.

839 Yuan, W., Xu, W., Ma, M., Chen, S., Liu, W., and Cui, L.: Improved snow cover model in terrestrial  
840 ecosystem models over the Qinghai–Tibetan Plateau, *Agric. For. Meteor.*, 218-219, 161-170,  
841 <https://doi.org/10.1016/j.agrformet.2015.12.004>, 2016.

842 Zeng, X., Wang, Z., and Wang, A.: Surface skin temperature and the interplay between sensible and  
843 ground heat fluxes over arid regions, *J. Hydrometeor.*, 13, 1359-1370,  
844 <https://doi.org/10.1175/JHM-D-11-0117.1>, 2012.

845 Zhang, G., Chen, F., and Gan, Y.: Assessing uncertainties in the Noah-MP ensemble simulations of  
846 a cropland site during the Tibet Joint International Cooperation program field campaign, *J.*  
847 *Geophys. Res.-Atmos.*, 121, 9576-9596, <https://doi.org/10.1002/2016jd024928>, 2016.

848 Zhang, H., Su, Y., Jiang, H., Chao, H., and Su, W.: Influence of snow subliming process on land-  
849 atmosphere interaction at alpine wetland, *J. Glaci. Geocry.*, 40, 1223-1230, 2018.

850 Zhang, T.: Influence of the seasonal snow cover on the ground thermal regime: An overview,  
851 *Reviews of Geophysics*, 43, RG4002, <https://doi.org/10.1029/2004RG000157>, 2005.

852 Zhao, L., Hu, G., Zou, D., Wu, X., Ma, L., Sun, Z., Yuan, L., Zhou, H., and Liu, S.: Permafrost  
853 changes and its effects on hydrological processes on Qinghai-Tibet Plateau, *Bull. Chin. Acad.*  
854 *Sci.*, 34, 1233-1246, <https://doi.org/10.16418/j.issn.1000-3045.2019.11.006>, 2019.

855 Zeng, X., Dickson, R., Barlage, M., Dai, Y., Wang, G., and Oleson, K.: Treatment of undercanopy  
856 turbulence in land models. *J. Clim.*, 18(23), 5086–5094. <https://doi.org/10.1175/Jcli3595.1>, 2005.

857 Zheng, D., van der Velde, R., Su, Z., Wen, J., Booij, M., Hoekstra, A., and Wang, X.: Under-canopy  
858 turbulence and root water uptake of a Tibetan meadow ecosystem modeled by Noah-MP, *Water*  
859 *Resour. Res.*, 51, 5735–5755. <https://doi.org/10.1002/2015WR017115>, 2015.

860 Zheng, D., van der Velde, R., Su, Z., Wen, J., and Wang, X.: Assessment of Noah land surface model  
861 with various runoff parameterizations over a Tibetan river, *J. Geophys. Res.-Atmos.*, 122, 1488-  
862 1504, <https://doi.org/10.1002/2016jd025572>, 2017.

863 Zheng, H., Yang, Z.-L., Lin, P., Wei, J., Wu, W.-Y., Li, L., Zhao, L., and Wang, S.: On the sensitivity  
864 of the precipitation partitioning into evapotranspiration and runoff in land surface  
865 parameterizations, *Water Resour. Res.*, 55, 95-111, <https://doi.org/10.1029/2017WR022236>,  
866 2019.

867 Zheng, W., Wei, H., Wang, Z., Zeng, X., Meng, J., Ek, M., Mitchell, K., and Derber, J.: Improvement  
868 of daytime land surface skin temperature over arid regions in the NCEP GFS model and its impact  
869 on satellite data assimilation, *J. Geophys. Res.-Atmos.*, 117, D06117,  
870 <https://doi.org/10.1029/2011jd015901>, 2012.

871 Zilitinkevich, S.: Non-local turbulent transport pollution dispersion aspects of coherent structure of  
872 convective flows, *Air Pollution III, Air pollution theory and simulation* (H Power, N  
873 Moussiopoulos, C A Brebbia, eds ) *Computational Mechanics Publ* , Southampton, Boston, 1, 53-  
874 60, 1995.

875 Zou, D., Zhao, L., Sheng, Y., Chen, J., Hu, G., Wu, T., Wu, J., Xie, C., Wu, X., Pang, Q., Wang, W.,  
876 Du, E., Li, W., Liu, G., Li, J., Qin, Y., Qiao, Y., Wang, Z., Shi, J., and Cheng, G.: A new map of  
877 permafrost distribution on the Tibetan Plateau, *The Cryosphere*, 11, 2527-2542,  
878 <https://doi.org/10.5194/tc-11-2527-2017>, 2017.

879